Relativistic Recirculating Planar Magnetrons

by

Matthew Alan Franzi

A dissertation submitted in partial fulfillment
of the requirements for the degree of
Doctor of Philosophy
(Nuclear Engineering and Radiological Sciences)
in The University of Michigan
2014

Doctoral Committee:

Professor Ronald M. Gilgenbach, Co-Chair
Professor Yue Ying Lau, Co-Chair
Professor John E Foster
Professor Brian Gilchrist

ACKNOWLEDGEMENTS

This research was supported by the Air Force Office of Scientific Research (grant number FA9550-10-1-0104), the Air Force Research Laboratory, and L-3 Communications. Special thanks is also given to acknowledge the Directed Energy Professional Society and their support through the Directed Energy Professional Society Graduate Scholarship. This project would not have been possible without the support and guidance of my advisors Professor Ronald Gilgenbach, and Professor Y. Y. Lau. Their enthusiasm for research, and seemingly limitless intellectual resources, created an incredible environment that I was fortunate enough to be a part of during my time at Michigan. Additionally, I would like to thank Dr. Brad Hoff of the Air Force Research Laboratory, whose advice, support, and collaborative research on the Recirculating Planar Magnetron were pivotal to the development of this project. Finally, I would like to extend my gratitude to Professor John Foster and Professor Brian Gilchrist, for serving on my committee, as well as my family, friends, and colleagues for all of their help and support

Contents

ACKNOWLEDGEMENTS . . . . . **ii**

Contents . . . . . **iii**

List of Figures . . . . . **vi**

List of Tables . . . . . **xxii**

LIST OF APPENDICES . . . . . **xxiii**

CHAPTER

I. Introduction 1

II. Theory of Planar Magnetron 7

2.1 Planar Diodes 7

2.1.1 Synchronism 9

2.1.2 Planar Resonance and Dispersion 13

2.1.3 Planar Magnetron Operation 22

III. Simulation and Design of the Recirculating Planar Magnetron 26

3.1 Design of the RPM-12a 26

3.1.1 Numerical Cold Tests: Solid Cathode 28

3.1.2 Numerical Cold Tests: Mode Control Cathode . . . 33

3.1.3 Electromagnetic Particle in Cell Modeling: Solid Cathode 39

3.1.4 Electromagnetic Particle in Cell Modeling: Mode Control Cathode 41

3.2 Extraction Concepts and Design 48

3.2.1 Coaxial to Waveguide Coupler Design 49

3.2.2 Proof of Principle Extractor 56

3.2.3 Coaxial All Cavity Extraction (CACE) 59

3.2.4 CACE Design 62

3.2.5 Particle in Cell Simulations of the RPM-340 CACE 73

IV. Experimental Configuration 77

4.1 Magnetron Anodes: Smoothbore 77

4.1.1 Solid Cathode Prototypes 79

4.2 Magnetron Anodes: RPM-12a 80

4.2.1 Cathodes: MCC-1 84

4.2.2 Cathodes: MCC-2 86

4.3 Extraction: Coaxial Proof of Principle 87

4.4 Distributed Field Adapter 88

V. Experimental Results 91

5.1 Smoothbore Magnetron 91

5.2 RPM-12a with LC-1 (Solid Cathode) 93

5.3 RPM-12a with Mode Control Cathode 99

5.3.1 MCC-1 Cathode 100

5.3.2 MCC-1L Cathode 103

5.3.3 MCC-1Lg Cathode 106

5.4 Overall Comparison of Cathodes on RPM-12a 109

5.5 Distributed Field Adapter: DFA-340e Testbed 111

5.6 RPM-12a Proof of Principle Coaxial Extractor 112

VI. Summary and Conclusions 121

6.1 Overview of the Recirculating Planar Magnetron 121

6.1.1 Numerical Summary 122

6.1.2 Experimental 123

6.1.3 RPM-340 CACE design 125

APPENDICES **127**

Bibliography **144**

List of Figures

1.1 Cylindrical A6 relativistic magnetron shown from the: a) front, and b) oblique perspective. 2

1.2 3D Solidworks renderings of each RPM embodiment including: A) Type (2) with cylindrical cavities, B) Type (2) with planar cavities, and C) Type (1) with planar cavities. 3

1.3 3D Solidworks renderings the RPM including: A) Oblique perspective of the Axial-B RPM, and B) Expanded view isolating each quadrant of the RPM anode. 4

2.1 Simple, planar diode displaying crossed-field configurations required for magnetron operation. 7

2.2 Simple, planar diode demonstrating: A) single particle cycloidal orbits, and B) shear velocity profile in Brillouin Flow. 8

2.3 Single particle interactions in an RF field for two particles at opposite phase depicting energy gain of the RF wave (green) and energy loss for the wave (red). 10

2.4 Buneman-Hartree curves for planar and cylindrical diodes depicting synchronism for a planar diode with a RF phase velocity of 0.25 c (solid blue) and the cylindrical diode with a RF phase velocity of 0.25 c (dashed blue). 13

2.5 2D representation of the Mode Control Cathode geometry in the RPM with: A) DC electric and magnetic fields as well as beam drift direction (shown in red), and B) RF electric field configuration. 15

2.6 Single period of the RPM slow wave structure with MCC showing the three regions of vacuum: I) the AK gap, II) the gap in the cathode, and III) the resonant cavity. The horizontal axis, $x = -h_2$, bisects the RPM into two halves. 16

2.7 Sample section of the RPM slow wave structure and solid cathode with arrows represent the direction and normalized magnitude and direction of the $\vec{E_{RF}} X \vec{B}$ drift experienced by the particles as well as the spoke formation caused by these drifts (shaded red). 23

2.8 Sample section of the RPM slow wave structure and MCC with arrows represent the normalized magnitude and direction of the $\vec{E_{RF}} X \vec{B}$ drift experienced by the particles as well as the spoke formation caused by these drifts (shaded red). . . 24

2.9 Simulated magnetron operation (in MAGIC PIC) of the RPM-12a with solid cathode for varying stages of mode development including: A) Initial electron emission (19 ns), B) Brillouin flow and electron hub formation (24 ns), C) RF perturbations on laminar flow (43 ns), and D) Full π-mode operation (60 ns). . 25

3.1 2D Simulation in MAGIC PIC of the initial L-band RPM-prototype. External magnetic field points out of the paper. 27

3.2 3D rendering of the RPM-12a in SolidWorks from front-on perspective (left) and oblique-perspective (right). 28

3.3 Infinite, planar cavity array for the solid cathode geometry represented by a single periodic structure with master/slave boundary conditions in HFSS. . . . 29

3.4 Electric field configurations for the even and odd $\frac{5\pi}{6}$-modes (left) and π-modes (right) found using HFSS. 31

3.5 Dispersion relation for the even modes of the RPM-12a as found using the analytic model (dashed-black), an infinite planar array in HFSS (black) and a finite 12 cavity geometry with fringe fields (blue X's). 32

3.6 Infinite planar cavity array for the MCC geometry represented by a single unit of the structure with master/slave boundary conditions in HFSS. 33

3.7 Dispersion relation including the mode control cathode for the even (dashed-black) and odd (black) modes using the analytic model compared to the even (dashed-blue) and odd (blue) modes in the infinite cavity array in HFSS. . . . 34

3.8 Analytic mode separation results between the even and odd pi-modes for: A) varying parameter (h2) and setting w2=0.024 m, AK=0.01 m, B) varying parameter (w2) and setting h2=0.002 m, AK=0.01 m, and C) varying parameter (b) and setting w2=0.024 m, h2=0.002 m. 35

3.9 Dispersion relation for: A) the RPM-12a using a solid cathode (black), as well as the even (dashed blue) and odd (x-blue) modes using the MCC-1 geometry, and B) a zoomed-in illustration of π-mode separation between the even and odd mode solutions. 37

3.10 Dispersion relation for the RPM-12a using the MCC-2 with the even (dashed purple) modes and odd (x-purple) modes. 38

3.11 A) An oblique 3D rendering of the RPM-12a simulated/experimental configuration made in Solidworks, and B) longitudinal (YZ) cross section of the simulated geometry in MAGIC PIC. 39

3.12 Velocity Profile of the the RPM-12a with LC-1 Cathode 10 ns prior to mode-startup as a function of (x), the distance from the horizontal axis of symmetry of the device, with specific emphasis on: A) the start of the Cathode, and B) The Virtual Cathode layer. 40

3.13 Applied voltage as a function of axial magnetic field required to reach Hull Cutoff (black), $5\pi/6$-mode (grey), π-mode (blue), and π mode with adjusted AK-gap due to virtual cathode (dashed-blue) for the RPM-12a with LC-1. 41

3.14 2D MAGIC PIC image of a dual reentrant magnetron operating in: A) π-mode using a solid cathode, B) even π-mode using a MCC, and C) odd π-mode using a MCC. 43

3.15 Simulated results of the simulated "reentrant planar magnetron" with MCC showing oscillation start up times (x) and phase locking times (dots) as a function of the AK gap. 44

3.16 A transverse cross section (XY) phase-space particle plot depicting even π-mode operation of the RPM-12a using the MCC-1 in MAGIC PIC. 45

3.17 Velocity Profile of the the RPM-12a with MCC-1 Cathode 10 ns prior to mode-startup as a function of (x), the distance from the horizontal axis of symmetry of the device, with specific emphasis on: A) the start of the Cathode, and B) The Virtual Cathode layer. 46

3.18 Analytic Hull cutoff (black) and Buneman Hartree curves for $\frac{5\pi}{6}$ (dashed) and π (blue) modes overlaid with the applied potential and magnetic field for even π-mode startup of the RPM-12a with rounded MCC-1 (X) in MAGIC PIC. . . 47

3.19 A transverse cross section (XY) phase-space particle plot depicting even π-mode operation of the RPM-12a using the MCC-2 in MAGIC PIC. 48

3.20 A) The cylindrical cross section DFA, B) the rounded rectangular cross section DFA, and C) the elliptical cross section DFA. 50

3.21 Longitudinal cross section (YZ) of the DFA-650c featuring the prominent dimensions used for design and fabrications. 51

3.22 Transmission properties of the DFA-650c with: A) S(2,1) as a function of frequency and target frequency band (shaded blue), and B) VSWR as a function of frequency. 52

3.23 A) Transverse cross section of the elliptical DFA with relevant dimensions, and B) Longitudinal cross section of the elliptical DFA with relevant dimensions shown in Table 3.2. 53

3.24 Transmission properties of the DFA-340e featuring the two-port S(2,1) parameter as a function of frequency for both a perfect conductor (blue) and a SS coupler (black). 54

3.25 Peak Electric field magnitude in the transmission line observed in HFSS as a function of input power. 55

3.26 A) An oblique 3D rendering of the PoP extractor simulated/experimental configuration made in Solidworks, and B) longitudinal (YZ) cross section of the simulated geometry in MAGIC PIC overlaid with a contour map representing E-field magnitude. 56

3.27 Simulated shot profile from MAGIC PIC illustrating voltage (blue), current (green), and extracted power (black) as a function of time. 57

3.28 Time integrated Fourier Transform of the oscillatory voltage signal within the extraction waveguide. 58

3.29 A 2D cross-section an all-cavity extraction anode using standard rectangular waveguide. 60

3.30 Theoretical peak efficiency for magnetron operation as a function of the device's RF phase velocity. 61

3.31 Mode Matched Converter: Oblique perspective of 3D model (top) and 2D transverse cross sections at varies stages (bottom). 63

3.32 Electric field configurations (arrows) for the RPM CACE for the: A) Transverse cross section, and B) Longitudinal cross section. 64

3.33 Plots correlating: A) the quality factor, and B) the pulled resonant frequency as a function of the length of the RPM coupling slot. 67

3.34 A) RPM-340CACE longitudinal cross section (XZ) illustrating the shorting plate offset (Z_1), B) The shift in resonant frequency of even and odd π-modes as a function of Z_1, and C) The shift in quality factor (Q) as a function of Z_1 for both the even and odd π-modes. 69

3.35 Dispersion relation for the RPM-CACE illustrating frequency for the even (dashed line) and odd (solid line) modes as a function of phase shift per cavity, obtained from HFSS. 70

3.36 Simulated DFAe in HFSS overlaid with contour maps illustrating the peak electric field for 100 MW input power. 72

3.37 A) Phase-space particle plot in ICEPIC representing pi-mode operation of the RPM-CACE with electrons (red) and conducting walls (black) and B) Voltage (dashed-blue), Current (green), Power (black), and Efficiency (dashed-black) as a function of time for the same simulated model. 74

3.38 A) Total extracted RMS Power, and B) efficiency from the RPM-340CACE as a function of slot length for a fixed width (1.1 cm) rectangular coupling slot. . . 75

4.1 Photograph of the interior of the Michigan Electron Long Beam Accelerator-Ceramic insulator (MELBA-C) Marx Bank. 78

4.2 Photographs of: A) the smoothbore RPM anode, and B) the full smoothbore assembly with the SC-1 cathode. 79

4.3 Photographs of: A) the LC-1 cathode and cathode stalk, and B) the full smoothbore assembly with the LC-1 cathode. 80

4.4 Photographs of the full RPM-12a assembly with the LC-1 cathode. 80

4.5 A) Experimental equipment diagram of the RPM-12a with diffraction coupling, and B) Exterior photograph of the experimental assembly in (A). 81

4.6 Photograph of the LC-1 with dielectric fiber emission priming sites. 82

4.7 Photograph of experimental B-dot loop on the central vane of the bottom oscillator of the RPM-12a. 84

4.8 Photographs of: A) the MCC-1 cathode and cathode stalk, and B) the full RPM-12a assembly with the MCC-1Lg (Glyptal coated). 85

4.9 Experimental photographs of damage caused by arcing to the cathode (left) and anode (right). 86

4.10 Photographs of: A) the MCC-2 cathode, and B) the RPM-12a assembly with the MCC-2 cathode. 87

4.11 A) Experimental equipment diagram of the RPM-12a with coaxial extraction, and B) exterior photograph of the experimental assembly in (A). 88

4.12 Photograph of the experimental test setup for the DFA-340e 89

5.1 Experimental shot profile for the smooth bore RPM and LC-1 cathode with Voltage (blue) and Current (green). 92

5.2 Experimental shot profile with Voltage (blue) and Current (green) for: A) the RPM-12a and LC-1 cathode, and B) The RPM-12a and LC-1 cathode with emission priming. 93

5.3 Experimental cold test data taken using the network analyzer equipped with a dipole antenna in close proximity to the RPM-12a cavities when installed in the vacuum chamber. 94

5.4 Buneman Hartree Curves for the RPM-12a π-mode (blue), $5\pi/6$-mode (red), and Hull cutoff (black) overlaid with the operational positions of each solid cathode shot (black x). 95

5.5 RPM-12a with LC-1 data: A) shot profile depicting voltage (green), current (blue), sampled power (black) as function of time, B) raw signal from heterodyne diagnostic, C) time-integrated Fourier transform, and D) time-frequency analysis (normalized white=1 and blue=0.5 and black=0). 96

5.6 RPM-12a with LC-1 data: A) shot profile depicting voltage (green), current (blue), sampled power (black) as function of time, B) raw signal from heterodyne diagnostic, C) time-integrated Fourier transform, and D) time-frequency analysis (normalized white=1 and blue=0.5 and black=0). 97

5.7 A) Raw data from B-dot signal on the top oscillator (blue) and the bottom oscillator (black), and B) relative phase difference between each B-dot as a function of time. 98

5.8 RPM-12a with LC-1: A) Raw data from the B-dot Signal on the top oscillator, and B) Time Frequency Analysis from the B-dot signal (normalized white=1 and blue=0.5 and black=0). 98

5.9 Experimental results from the RPM-12a with MCC-1 showing: A) Raw data from B-dot signal on the top oscillator (blue) and the bottom oscillator (black), and B) relative phase difference between each B-dot signal as a function of time. 99

5.10 Zoomed in plots from Fig. 5.9A with the RPM-12a and MCC-1 depicting: A) Raw data from B-dot signal on the top oscillator (blue) and the bottom oscillator (black) during a state of phase-locked operation with a relative phase 70 degrees, and B) Raw data from B-dot signal on the top oscillator (blue) and the bottom oscillator (black) during a state of phase-locked operation with a relative phase 0 degrees. 100

5.11 RPM-12a with MCC-1 Buneman Hartree Curves for: π-mode (blue), $5\pi/6$-mode (grey), and Hull cutoff (black) overlaid with the operational parameters of each shot using the RPM-12a with MCC-1 (blue x). 101

5.12 Comparison of average phase locked duration for relevant RPM-12a shots between the MCC-1 and the LC-1 for locking criteria of 5, 10, and 15 degrees. . . 102

5.13 Average microwave pulselength for the RPM-12a with LC-1 and MCC-1 cathodes. 103

5.14 RPM-12a Buneman Hartree Curves for: pi-mode (blue), 5pi/6-mode (grey), and Hull cutoff (black) overlaid with the operational parameters of each shot using the RPM-12a with MCC-1L (green x). 104

5.15 Comparison of average phase locked duration for relevant shots on the RPM-12a using the MCC-1L and the LC-1 for locking criteria of 5, 10, and 15 degrees. . 105

5.16 Average microwave pulselength for the RPM-12a using the LC-1 and MCC-1L cathodes. 105

5.17 RPM-12a Buneman Hartree Curves for: pi-mode (blue), 5pi/6-mode (grey), and Hull cutoff (black) overlaid with the operational parameter of each shot of the RPM-12a with MCC-1Lg (red x). 106

5.18 Relative startup time referenced to an applied voltage of 175 kV for the RPM-12a using: the solid cathode (grey), MCC-1 (blue), MCC-1L (green), and MCC-1Lg (red). 107

5.19 Comparison of average phase locked duration for relevant shots between the RPM-12a with the MCC-1L and the LC-1 for locking criteria of 5, 10, and 15 degrees. 108

5.20 Average microwave pulse length for the RPM-12a using LC-1 and MCC-1L. . . 109

5.21 Operational frequency for each experimental shot on the RPM-12a as a function of applied magnetic field for the solid cathode (black) and MCC (blue). 110

5.22 Sampled power measurements for the RPM-12a using a solid cathode (black), MCC-1 (blue), MCC-1L (green), MCC-1Lg (red), MCC-2 (purple). 110

5.23 Transmission properties of the DFA-340e, comparing a simulated single DFA-340e made from perfect conductors (..), a simulated single coupler made from SS-304 (x), two simulated couplers adjoined together made from SS 304 (–), and two adjoined couplers made from SS304 in experiment (-). 112

5.24 Experimental configurations of the RPM-12a with PoP extractor. 113

5.25 Shot profile for the horizontally-oriented RPM-12a with MCC-2 and PoP extractor depicting voltage (blue), current (green), and total microwave power (black) as a function of time. 114

5.26 RF signal from the WR-650 directional loop couplers as measured from the top (black) and bottom (blue) waveguides in the PoP extractor on the horizontally-oriented RPM-12a. 115

5.27 Comparison of average phase locked duration for relevant shots on the vertically oriented RPM-12a with PoP extractor using the MCC-2 and the RPM-12a with LC-1 for locking criteria of 5, 10, and 15 degrees. 115

5.28 Experimental results for the vertical configuration of RPM-12a with PoP extractor and MCC-2 depicting: A) Extracted microwave power as a function of shot number, and B) applied magnetic field as a function of shot number. 117

5.29 Shot profile for the RPM-12a with MCC-2 and PoP extractor depicting voltage (blue), current (green), output microwave power from the left-oscillator (dashed red), and output microwave power from the right-oscillator (black) as a function of time. 118

5.30 Experimental results for RPM-12a with PoP extractor and MCC-2 depicting: A) Extracted microwave power as a function of operating frequency, and B) instantaneous peak efficiency as a function of operating frequency for both the vertical (blue-X) and horizontal (black-O) configurations. 119

5.31 Dominant operating frequency observed in experimental runs of the RPM-12a with PoP extractor as a function of applied magnetic field for both the vertical (blue-X) and horizontal (black-O) configurations. 120

A.1 Experimental schematic drawings of the RPM-12a (cm). 129

A.2 Experimental schematics for the LC-1 solid cathode include: A) 3D-Solidworks rendering, and B) dimensions of the LC-1 (cm). 130

A.3 Experimental schematics of the MCC-1 including: A) primary dimensions of the MCC-1 (cm), B) 3D Solidworks rendering of the MCC-1, and C) 3D Solidworks rendering of a single MCC endhat. 131

A.4 Experimental schematic of the MCC-2 including: A) primary dimensions of the MCC-2 (cm), B) 3D Solidworks rendering of a partially assembled MCC-2, and C) 3D Solidworks rendering of the MCC-2 (exploded perspective). 132

B.1 RPM-340CACE with: A) Main body up through the coaxial tranmission lines, and B) main body up through WR340 waveguide and C) Complete RPM-340 CACE assembly. 134

B.2 Experimental schematic of the RPM-340 including: A) 3D Solidworks rendering of the RPM-340, and B) primary dimensions of the RPM-340 (cm). 135

B.3 Experimental schematic of the MCC-3 including: A) 3D Solidworks rendering of the MCC-3 (exploded perspective), and B) primary dimensions of the MCC-3 (cm). 136

B.4 A) Oblique 3D cross-section of the RPM CACE, and B) 2D longitudinal (XZ) cross-section of the RPM CACE. 137

B.5 Experimental photo of RPM-340 CACE Anode (Pre-assembly) 138

C.1 A) Transverse (XY) cross section of a planar, rising sun, variant operating in π-mode that includes the MCC and CACE system, and B) simulated shot profile showing voltage, current, power and efficiency as a function of time. 141

C.2 1) Top-down perspective of: a) solid cathode, b) standard MCC, and c) a magnetically primed MCC; 2) magnetic field profile on the surface of the cathode due to axial current of 1 kA. 142

C.3 Transverse (XY) cross section of the electrically primed MCC. 143

List of Tables

3.1 Proof of Principle Mode Control Cathode dimensions. 42

3.2 Optimized dimensions of the DFA-340e for transmission and minimal electric field magnitude from 1.85 to 2 GHz. 56

3.3 Peak Electric Field Magnitudes on the DFA-340e coupler at various point axially along the transmission line. 72

LIST OF APPENDICES

Appendix

A. Schematics for the RPM-12a and Cathodes 128

B. RPM-340 CACE Schematics 133

C. Planar Adaptations of Cylindrical Magnetron Concepts 139

CHAPTER I

Introduction

Magnetrons are efficient microwave generators, whose versatility and robust operation facilitate their extensive use in both military and commercial operations. This compact crossed-field device is well suited for applications such as radar, counter-electronics, long range communication, and commercial heating [1–4]. Cylindrical relativistic magnetrons are of particular interest since advancements in modern pulsed power supplies and fabrication techniques have led to immense improvements of these devices, which are capable of producing high power microwave (HPM) pulses of 0.1 to 4 GW in output power with efficiencies up to 35 % for pulse lengths in the range of 0.1 to 1 μs [5–7]. Simulated models of relativistic magnetrons, using modern computing and numerical software, have demonstrated efficiencies as high as 50 to 70 % [8, 9]. Many modern relativistic magnetrons [5] are adapted from the cylindrical achitechture of the A6, illustrated in Fig. 1.1, a six cavity magnetron developed at MIT in the late 1970's for its high power output and efficiency [10].

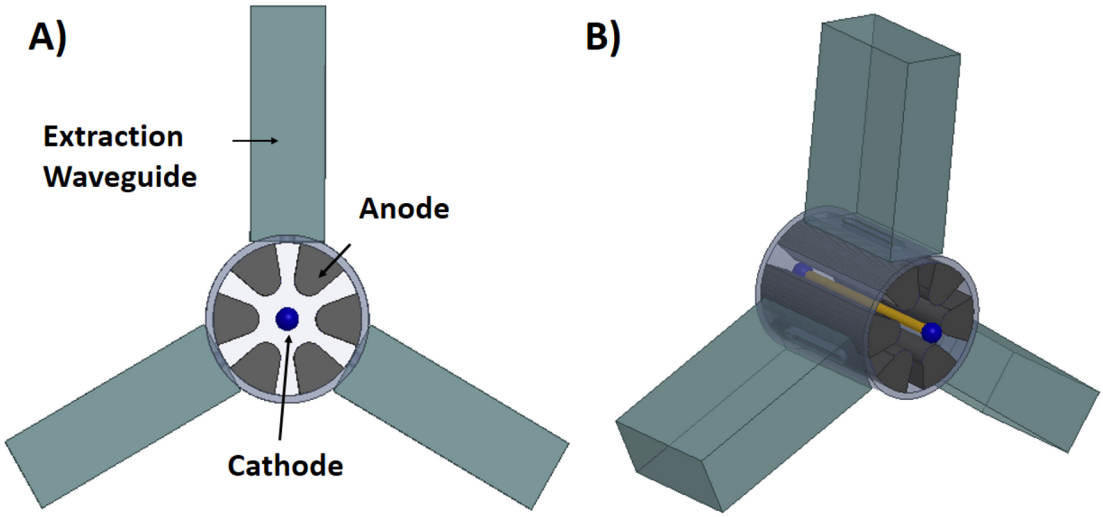

Figure 1.1. Cylindrical A6 relativistic magnetron shown from the: a) front, and b) oblique perspective.

Ongoing research on this device includes seeding mode development with techniques such as magnetic, emission, and RF priming, which have contributed significantly to both faster start up and higher net efficiency [11–20]. Cylindrical diodes, operating in a space charge limited regime, are subject to limited diode currents due to restricted cathode surface area [1, 21]. Low diode currents limit both average and peak output power. Low impedance, high current, structures can be attained but at cost of a significant increase in cross sectional area, number of cavities, and volume of magnetic field [3]. Conversely, inverted magnetrons are comparatively limited in anode area which hampers heat removal and the number of viable power extractors [22]. Planar magnetrons, which provide large surface areas and ideal power/volume scaling, are inefficient in comparison due to lack of recirculation and substantial losses in beam dumps or collectors. The Recirculating Planar Magnetron (RPM) [23] is a crossed-field device that combines the advantages of high-efficiency recirculating devices with

those of planar devices: both large-area cathode (high current) and anode (improved thermal management). Additionally, the magnetic field volume of the RPM scales with N as compared to N^2 for cylindrical magnetron, where N is the number of cavities [24]. Manifestations of the RPM concept can be categorized into two classifications which are distinguished by their applied crossed-field configurations. These two configurations of the RPM include:

1. Axial magnetic field with radial electric field, and
2. Radial magnetic field with axial electric field.

Each crossed-field configuration has geometric variations with their unique conditions for resonance and synchronism within the magnetron. Three geometric embodiments are illustrated in Fig. 1.2(A-C). Figure 1.2A is a type (2) configuration with a cylindrical cavity array, Fig. 1.2B is a type (2) configuration with the planar cavity array, and Fig. 1.2C is a type (1) configuration with a planar cavity array.

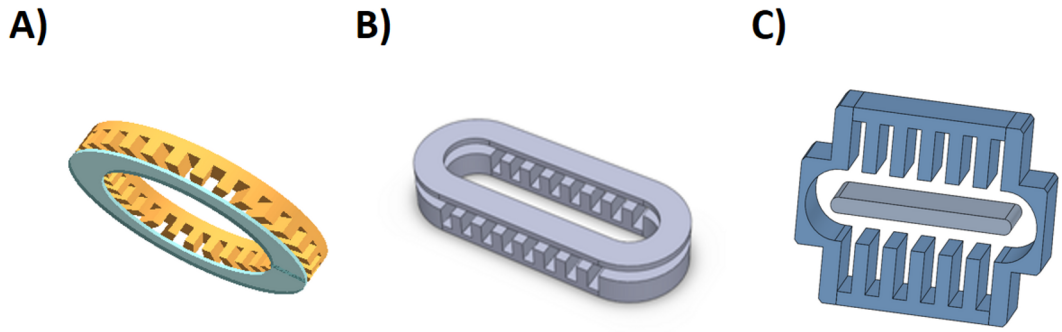

Figure 1.2. 3D Solidworks renderings of each RPM embodiment including: A) Type (2) with cylindrical cavities, B) Type (2) with planar cavities, and C) Type (1) with planar cavities.

The field configuration of type (1) was first proposed independently by Brown, as a traveling wave device, and by Kapitza, as the Planotron, in the early 1960's [25, 26].

A related study was performed using Particle in Cell (PIC) codes and applying "reentrant" boundary conditions in a 2D planar magnetron [27–29]. The radial B-field planar magnetron (2) was presented by Harrowell in 1984 [30], who described the possibility of using cusp magnets.

The primary focus of this thesis will be the validation of the RPMs dispersion relation and operational feasibility through theory and experiment using the embodiment with the type (1) axial field configuration and planar cavity array depicted in Fig. 1.2C. The axial B RPM anode (referred to as "RPM" henceforth) consists of four distinct structural elements: two planar slow wave structures with rectangular cavities and two smoothbore, adjoining cylindrical sections, as illustrated in Fig. 1.3(A-B).

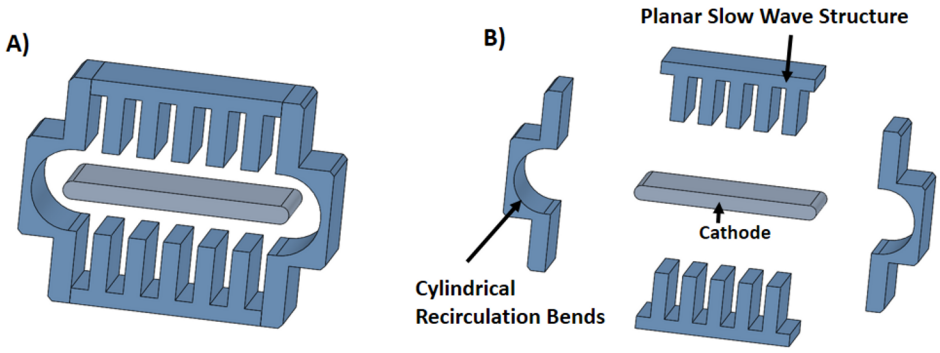

Figure 1.3. 3D Solidworks renderings the RPM including: A) Oblique perspective of the Axial-B RPM, and B) Expanded view isolating each quadrant of the RPM anode.

The planar slow-wave structure is simplified to periodic rectangular cavities equally-spaced between rectangular vanes, designed to support a π-mode electric field configuration as it has been demonstrated to be the most efficient operating mode within a magnetron [1, 3, 4]. The two resonant arrays, which are predominantly isolated by

the conducting boundary at the cathode, are only coupled at either end of the device by the cylindrical smooth-bore sections. Fundamentally, these adjoining regions are designed to preserve beam current, allowing current that exits one planar structure to "recirculate" and enter the other. More complex recirculation geometries could provide efficient beam recirculation while matching the RF phase velocity to the planar slow wave structure over this path length. Phase matched geometries have been proposed using cylindrical slow wave structures, increased cylindrical diode separation (AK gap), and using cylindrical resonant cavities instead of a smoothbore geometry (or some combination thereof). These more advanced techniques, however, would considerably increase the complexity of the device [24].

The smooth-bore recirculation geometries, presented in this thesis, have a simplified geometry that resembles the models used to determine analytic beam dynamics. Despite their structural simplicity and ease of fabrication, these smooth bore geometries often fail to maintain complete synchronism of space charge bunches from one oscillator to the other. The "detuned" electron beam must then "re-bunch" as it traverses through each planar slow-wave structure, heavily mitigating the influence of the RF power generated from the opposing side. The partially isolated oscillators often fail to achieve a global locked-mode during operation and instead exhibit mode competition and beating between each oscillator. Preliminary investigations of the RPM have demonstrated that the device is susceptible to weak electromagnetic coupling between the two planar slow-wave structures which might cause several deleterious phenomena such as cross-oscillator mode competition and incoherency between oscillators. [31].

These issues are addressed by increasing both the frequency separation between adjacent modes as well as the RF "communication" between oscillators, thereby

enhancing the propensity of the RPM to startup and lock into a single mode of operation [32].Mode separation in a cylindrical magnetron is addressed most conveniently through strapping [33] or using an anode containing a rising sun resonant cavity configuration [3, 34]. Anode strapping in the relativistic regime is generally not realistic due to the proximity of the conductive straps to the anode vanes which, during operation, may generate large potentials that can initiate RF-breakdown [10]. Rising sun magnetrons, which house cavities of alternating resonant frequencies, allow for greatly enhanced separation between π-mode and $(\pi - 1)$-modes [35–37].Frequency separation between operating modes of the planar slow-wave structure is described analytically in Chapter 2 and numerically in Chapter 3. Planar variants of the rising sun anode configuration are not considered for the preliminary investigation of the RPM anode. Alternatively, simulated results in Chapter 3 detail several techniques of introducing mode separation well suited for a planar geometry including novel cathode designs and RF power extraction techniques. RF communication and locking within the RPM are evaluated in numerical simulation in Chapter 3 and experimentally in Chapters 4 and 5. Schematics for the RPM-12a, LC-1, MCC-1, and MCC-2 are found in Appendix (A). The analytic, simulated, and experimental development of a new RPM class is discussed in Chapter 3 and Appendix (B). The design, operation, and evolution of the RPM to date are summarized in Chapter 6.

CHAPTER II

Theory of Planar Magnetron

2.1 Planar Diodes

The operation of a magnetron is a highly complex process which defies a purely analytic description to this date [2]. Simplification of both the device's geometry and the electron dynamics are often required to provide some basic understanding of numerical and experimental results. This simplification is accomplished by assuming the magnetron composed of an infinite smooth-bore planar diode as shown in Fig. 2.1.

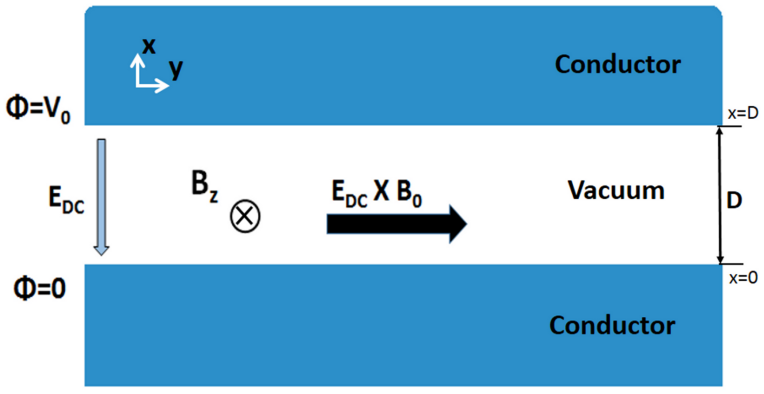

Figure 2.1. Simple, planar diode displaying crossed-field configurations required for magnetron operation.

In this model, the planar diode is subject to externally applied electric and magnetic fields in a crossed-field configuration. Electrons are emitted into the gap. The presence of the axial magnetic field will cause the particles to undergo cycloidal orbits as illustrated in Fig. 2.2A. Another model of the orbits is the laminar flow, known as Brillouin flow, shown in Fig. 2.2B [38, 39].

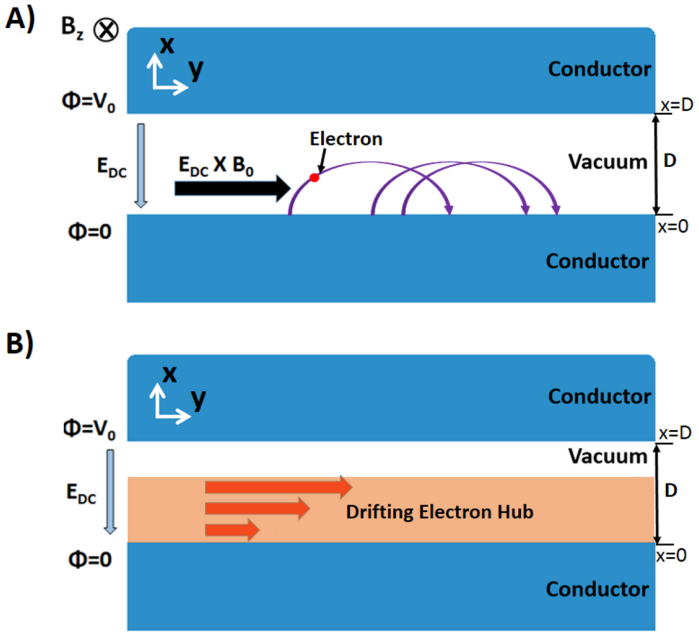

Figure 2.2. Simple, planar diode demonstrating: A) single particle cycloidal orbits, and B) shear velocity profile in Brillouin Flow.

Further simplification of the single particle orbit (Fig. 2.2A) can be made by ignoring space charge effects and assuming that an electron is emitted from the cathode with a zero initial velocity ($v_0 = 0$). The resultant , non-relativistic, force law for single particle orbits in Cartesian coordinates is given by,

$$m\frac{dv_x}{dt} = -e(E + v_y \times B), \tag{2.1}$$

$$m\frac{dv_y}{dt} = e(v_x \times B). \tag{2.2}$$

By integrating Eq. 2.2 with respect to time, a relation is obtained for the transverse velocity as a function of $\hat{x}$ where ($\omega_c = \frac{eB}{m}$).

$$v_y(t) = \omega_c x \tag{2.3}$$

Energy conservation yields

$$0 = \frac{1}{2}(mv_x^2 + mv_y^2) - e\Phi = \frac{1}{2}m(v_x^2 + (\omega_c x)^2) - e\Phi \tag{2.4}$$

where Φ is the electrostatic potential. Magnetic insulation occurs if the particle tangentially grazes the anode at the apex of its cycloidal trajectory such that at $x = D$,$v_x = 0$, and $\Phi = V_0$, yielding,

$$0 = \frac{m}{2}(\omega_c D)^2 - V_0 e. \tag{2.5}$$

Assuming a fixed applied potential (V_0), the magnetic field required to achieve insulation, reads

$$B_H = \sqrt{\frac{2mV_0}{eD^2}}, \tag{2.6}$$

which is known as the Hull cutoff magnetic field.

2.1.1 Synchronism

In the planar diode field configuration, one may now include a resonant slow-wave structure to support the development of an RF wave during operation. The principal means of energy transfer within the magnetron may be explored by considering the single particle orbit trajectories of two electrons at dissimilar phases with respect to the wave [2, 4]. Examining Fig. 2.3, there are two electrons underneath adjacent cavities denoted in "red" and in "green". Here, the slow-wave structure is assumed to

operate in π mode such that the RF fields in neighboring cavities are out of phase by exactly π radians or 180 degrees.

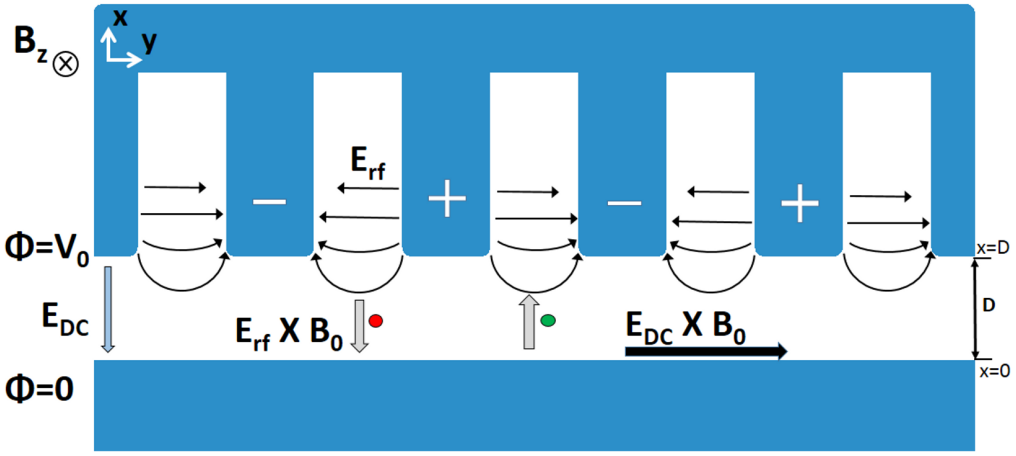

Figure 2.3. Single particle interactions in an RF field for two particles at opposite phase depicting energy gain of the RF wave (green) and energy loss for the wave (red).

The "green" electron is subject to a decelerating RF field of the cavity in the $\hat{y}$ direction causing it to give up its kinetic energy to the wave. Simultaneously, the particle will experience a drift in the positive $\hat{x}$ direction due to the $\vec{E_{RF}} X \vec{B}$ fields, into regions of higher E_{RF} and consequently larger decelerating forces. The loss in potential energy, as the green electron moves closer to the anode, is also given to the RF wave. Conversely the "red" particle will be accelerated by the RF field and take energy from the wave but is subject to an $\vec{E_{RF}} X \vec{B}$ drift in the $-\hat{x}$ direction where the RF fields are lower and the accelerating force is also lower. Overall, particles that are in the proper phase to give energy to the wave are exposed to stronger fields and the net transfer of energy is positive for the RF wave. The "phase focusing" mechanism also tends to convert the "red" particle into a green particle, thereby

making magnetron efficiency as high as 90 % [2](the self-focusing effect is shown in greater detail in Fig. 2.7 below). The optimal environment for the applied potential to transfer energy to the RF wave in this manner exists when the drifting electron beam achieves a velocity equal to that of the wave's phase velocity, satisfying a condition known as synchronism.

The synchronism condition for the planar geometry is most conveniently derived using the Brillouin flow model shown in Fig. 2.2B. At fixed value gap spacing (D), voltage (V_0), and magnetic field B ($> B_H$), the Brillouin flow is a rectilinear shear flow extending from ($x = 0$) at the cathode to ($x = h$) at the hub height [39–41]. Within the Brillouin hub ($0 < x < h$),

$$v_y = \omega_c x, \tag{2.7}$$

$$\Phi(x) = \frac{m}{2e}(\omega_c x)^2, \tag{2.8}$$

$$E(x) = -\frac{d\Phi}{dx} = -\frac{m}{e}\omega_c^2 x, \tag{2.9}$$

the electron density n_0 is a constant, satisfying $\omega_p = \omega_c$ where $\omega_p = (e^2 n_0/(m\epsilon_0))^{1/2}$ is the plasma frequency. The hub height (h) may be found from

$$V_0 = \Phi_{x=h} - E_{x=h}(D-h) = \frac{m}{2e}(\omega_c h)^2 + \frac{m}{e}\omega_c^2 h(D-h), \tag{2.10}$$

which is a quadratic polynomial in h. Solving this quadratic polynomial,

$$h = D - \sqrt{D^2 - 2\frac{V_0 e}{m\omega_c^2}} \tag{2.11}$$

The synchronism condition requires that the electrons at the top of the Brillouin hub are synchronized with the phase velocity (v_ϕ) of the circuit wave at this point. This condition implies,

$$\omega_c h = v_\phi \tag{2.12}$$

Substituting Eq. (2.11) into (2.12), the following relation between (V_0, B, D, v_ϕ) can be found,

$$V_0 = BDv_\phi - \frac{m}{2e}v_\phi^2. \tag{2.13}$$

V_0, as given by the RHS of Eq. 2.13, is also known as the Buneman-Hartree (B-H) voltage. The inclusion of relativistic effects for the planar diode modifies both the Hull Cutoff and BH synchronism equations to the following relations [2, 40, 42]:

$$V_{Hull} = \frac{mc^2}{e}[\sqrt{1 + \frac{(eBD)^2}{mc^2}} - 1], \tag{2.14}$$

$$V_{BH} = BD(\beta c) - \frac{mc^2}{e}[1 - (1 - \beta^2)]^{\frac{1}{2}}, \tag{2.15}$$

where $\beta = v_\phi/c$. Consideration of the cylindrical drift velocity and Hull cutoff are important in understanding the properties of the electron beam as it "recirculates" or drifts from one oscillator to the other in the cylindrical bends in the device. Additionally, the inclusion of cylindrical cavities, while not addressed in this body of work, has been proposed as a means to generate a continuous slow wave structure with fixed guided wavelength [24]. In cylindrical coordinates the Hull cutoff and B-H relations become [2, 6, 42–45]:

$$B_{Hull} = \frac{mc}{e(\frac{r_a^2 - r_c^2}{2r_c})}[2\frac{eV}{mc^2} + (\frac{eV}{mc^2})^2]^{\frac{1}{2}} \tag{2.16}$$

$$V_{BH} = B\beta c(\frac{r_a^2 - r_c^2}{2r_c}) - \frac{mc^2}{e}[1 - (1 - \beta)^2]^{\frac{1}{2}}, \tag{2.17}$$

where r_a and r_c are respectfully the anode and cathode radius. The applied fields necessary for synchronism in a cylindrical diode can differ greatly from that of the

purely planar geometry. The applied fields, as dictacted by the B-H relations in Eqs. 2.17 and 2.15, are compared in Fig. 2.4 for a cylindrical and planar diode respectfully. Each evaluated diode has a RF phase velocity of 0.25 c and a 3 cm AK gap. The cylindrical diode is assumed to have dimensions equivalent to the L-band A6 magnetron where $r_b = 8.75$ cm and $r_a = 0.625$ cm. According to the Fig. 2.4, given an applied voltage of -300 kV, an applied magnetic field of 0.21 T is required to achieve synchronism with the cylindrical slow-wave-structure while approximately 0.12 T is required for the planar diode. The RPM, which contains both cylindrical and planar regimes, must adjust either the radii of the cylindrical bends or the AK gap between the two regions accordingly to achieve equal $\vec{E}X\vec{B}$ drift velocities at the top of the electron hub.

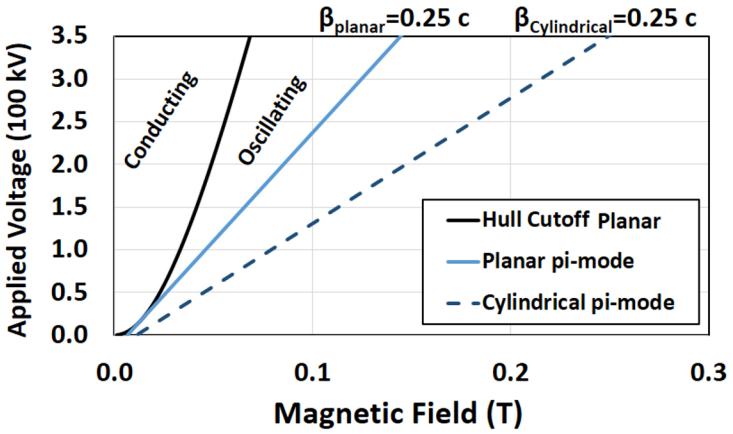

Figure 2.4. Buneman-Hartree curves for planar and cylindrical diodes depicting synchronism for a planar diode with a RF phase velocity of 0.25 c (solid blue) and the cylindrical diode with a RF phase velocity of 0.25 c (dashed blue).

2.1.2 Planar Resonance and Dispersion

The design of the resonant structure is critical in determining the operation criteria for the magnetron itself as it directly determines the resonant frequency and

phase velocity of the device. The Recirculating Planar Magnetron (RPM), shown in Fig. 1.3, presents a particularly complicated dispersion analysis as the existence of two, coupled, planar, cavity arrays introduces a bifurcated mode structure [31].

In a simple cylindrical cavity array, degenerate or phase-shifted equivalent modes are identical due to the symmetry of both the device and the mode [3]. The RPM, in contrast, has a single axis of symmetry which bisects the device in the transverse ($\hat{y}$) direction. Phase-shifted modes, which are no longer fully symmetric but have the same planar propagation constant experience a spread in frequency due to the dissimilar boundary conditions along this axis. The resultant mode structure contains two distinct sets of classic planar operating modes. These modes are more conveniently identified as either even-modes, which demonstrate a 0 degree phase shift between top and bottom oscillator, or odd-modes, which experience 180 degree phase shift.

The frequency separation experienced between even and odd modes is typically very low ($\delta f < 1\%$) for the standard RPM configuration, where the only dissimilarity between these phase shifted modes exists in the cylindrical recirculation bends. Closely spaced even and odd modes can lead to intense competition and mode degradation during the operation of the RPM. An approach to increasing the separation within the split mode structure is presented in the Mode Control Cathode (MCC) [32].

The fundamental MCC configuration, in Fig. 2.5, is an array of rectangular conductors that matches vane-cavity periodicity of the RPM, which intrinsically provide emission priming [11]. This MCC configuration is geometrically similar to a linear version of the Transparent Cathode (TC) [46]; TC is a device shown to improve start up time in relativistic cylindrical magnetron by not shorting out the DC com-

ponent of the azimuthal field. The MCC however differs from the TC because it acts as an *resonant electromagnetic device* that provides several additional benefits which enhance the operation of the RPM. These benefits include the potential to resonantly propagate RF power and electron bunches between oscillators, increased cross-oscillator communication, and the ability to tune the global mode structure of the RPM independently from the surrounding anode. The MCC is particularly well suited for increasing mode separation between the closely spaced even and odd modes. The differences in electromagnetic field configurations between the mode sets lie predominantly along the horizontal axis of symmetry on which the MCC is typically aligned. The MCC exploits this property by altering the boundary condition for each mode set in a periodic fashion throughout the entirety of the device.

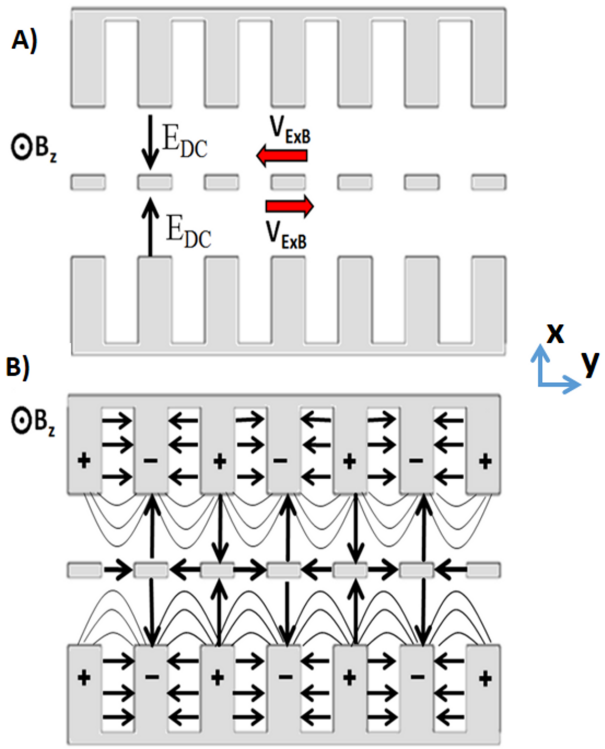

Figure 2.5. 2D representation of the Mode Control Cathode geometry in the RPM with: A) DC electric and magnetic fields as well as beam drift direction (shown in red), and B) RF electric field configuration.

This complicated geometry may be solved for analytically by adapting the classic approach of solving for the dispersion relation in an infinite planar cavity array [47, 48]. The approach utilizes a single vane-cavity structure (from $y = -L/2$ to $y = L/2$) shown in Fig. 2.6, and applies the Floquet Theorem to replicate the infinite array of period (L). The resonant frequency is obtained by first decomposing the area into three distinct regions of vacuum and identifying the electromagnetic fields for each region. These regions are designated as:

I -AK Gap: Vacuum region between cathode and anode,

II -Cathode Space: Vacuum region within the interior of the cathode, and

III -Resonant Cavity: Vacuum region with the interior of the anode.

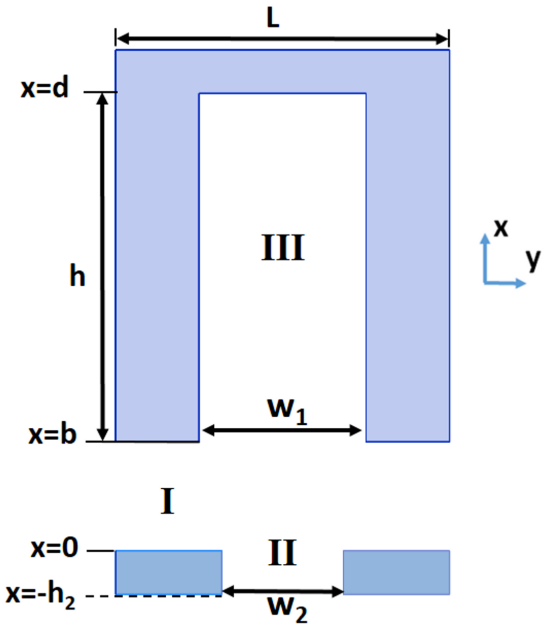

Figure 2.6. Single period of the RPM slow wave structure with MCC showing the three regions of vacuum: I) the AK gap, II) the gap in the cathode, and III) the resonant cavity. The horizontal axis, $x = -h_2$, bisects the RPM into two halves.

The electromagnetic fields of each region must be solved. The solutions are then used to match the RF fields along the two boundaries at (x=0) and (x=b) [32].

Region-I, $0 < x < b$ **and** $-L/2 < y < L/2$

The electric field in the AK gap is written in its most general form for the TM mode in the **x-y** plane,

$$H_z = e^{j\omega t} \sum_{n=-\infty}^{\infty} [A_n cosh(\gamma_n x) + A'_n sinh(\gamma_n x)] e^{-j\beta_n y}, \tag{2.18}$$

$$j\omega\epsilon E_x = -j e^{j\omega t} \sum_{n=-\infty}^{\infty} \beta_n [A_n cosh(\gamma_n x) + A'_n sinh(\gamma_n x)] e^{-j\beta_n y}, \tag{2.19}$$

$$j\omega\epsilon E_y = -e^{j\omega t} \sum_{n=-\infty}^{\infty} [A_n \gamma_n sinh(\gamma_n x) + A'_n \gamma_n cosh(\gamma_n x)] e^{-j\beta_n y}, \tag{2.20}$$

where $\beta_n = \beta_0 + 2n\pi/L$; $n = 0, \pm 1, \pm 2, ...$

Region-II, $-h_2 < x < 0$ **and** $-w_2/2 < y < w_2/2$

It is postulated that the electromagnetic fields in region II are the TEM modes shown in Eqs. 2.21 and 2.22 as they are the only important components for magnetron operation; (this TEM mode assumption will also be applied in Region-III).

$$E_y = B' sin(\frac{\omega(x + h_2)}{c}) + B cos(\frac{\omega(x + h_2)}{c}) \tag{2.21}$$

$$-j\omega\mu H_z = \frac{\omega}{c}[B' cos(\frac{\omega(x + h_2)}{c}) - B sin(\frac{\omega(x + h_2)}{c})] \tag{2.22}$$

The two fold symmetry of the RPM necessitates a unique boundary condition along the bisecting line at $x = -h_2$, essentially determining the manner by which electromagnetic field energy propagates from the top side of the device to the bottom side. This condition may be further categorized as a perfect E_y (null) boundary, corresponding to the odd mode solution set and 180 degree phase shift in E_y across

$x = -h_2$, or a perfect H_z (null) boundary, corresponding to the even mode solution set, (with E_y at a maximum at $x = -h_2$ and 0 degree phase shift in E_y across $x = -h_2$.

Region-III, $b < x < d$ **and** $-w_1/2 < y < w_1/2$

It is assumed that a TEM mode exists within each cavity, Region-III, an oft-used assumption [48].

$$E_y = e^{j\omega t} D sin(\frac{\omega(x-d)}{c}) \tag{2.23}$$

$$-j\omega\mu H_z = e^{j\omega t} \frac{D\omega}{c} cos(\frac{\omega(x-d)}{c}) \tag{2.24}$$

Even Mode Solutions

The degeneracy experienced by the RPM can be isolated (to either the even or the odd mode) analytically by the boundary condition applied at the horizontal plane of symmetry (x=-h_2). The even mode, whose electric field vector E_{yII} experiences a local maxima, satisfies $dE_y/dx = 0$ at $x = -h_2$. Applying this boundary condition to the TEM solution presented in Eq. 2.21 and Eq. 2.22 we can obtain the following,

$$E_{yII} = B cos(\frac{\omega(x+h_2)}{c}) \tag{2.25}$$

$$-j\omega\mu H_{zII} = -B\frac{\omega}{c} sin(\frac{\omega(x+h_2)}{c}) \tag{2.26}$$

Treating the cavity as a shorted parallel plate transmission line, the RF field at the vane tips reads,

$$E_{yIII} = -D sin(\frac{\omega h}{c}) \tag{2.27}$$

Resonance is achieved by matching the impedance at each interface (I-II and I-III). Classically this impedance matching is performed by ensuring continuity of the point-wise electric field E_y and average magnetic field B_z across the boundary. The RF electric fields in the AK gap (region I) is represented as a summation of an infinite combination of spatial harmonics in Eq. 2.19 must therefore be set equal to the value of the of the cavity field (E_{yIII}) at the I-III interface (x=b),

$$-Dsin(\frac{\omega h}{c}) = -\sum_{n=-\infty}^{\infty} \frac{\gamma_n}{j\omega\epsilon}[A_n sinh(\gamma_n b) + A'_n cosh(\gamma_n b)]e^{-j\beta_n y + j\omega t}. \tag{2.28}$$

Applying Fourier analysis over the period (L) the following expression relating the coefficients (A_n, A'_n, D) is obtained. Let:

$$D\frac{w_1}{L}sin(\frac{\omega h}{c})sinc(\theta_1) = -\frac{\gamma_n}{j\omega\epsilon}[A_n sinh(\gamma_n b) + A'_n cosh(\gamma_n b)], \tag{2.29}$$

where $sinc(x) = sin(x)/x$, $\theta_1 = \beta_n w_1/2$, and $\theta_2 = \beta_n w_2/2$.

In a similar fashion E_y must also be continuous across the I-II boundary at $x = 0$, relating (A'_n, B). From Eq. 2.20 and Eq. 2.25,

$$\frac{-\gamma_n}{j\omega\epsilon}A'_n = B\frac{w_2}{L}cos(\frac{\omega h_2}{c})sinc(\theta_2). \tag{2.30}$$

The average magnetic field, H_{zI} and H_{zIII}, must be equal across the I-III interface which is performed by integrated with respect to (y) from $y = L/2$ to $y = -L/2$ and dividing by the total distance (L) at $x = b$. Equation 2.31 relates the coefficients (A_n,A'_n, D),

$$\frac{-D}{j\mu c}cos(\frac{\omega h}{c}) = \sum_{n=-\infty}^{\infty}[A_n cosh(\gamma_n b) + A'_n sinh(\gamma_n b)]sinc(\theta_1). \tag{2.31}$$

Applying the same analysis to the magnetic field across the I-II boundary at $x = 0$, relating (A_n, B).

$$\frac{B}{j\mu c} sin(\frac{\omega h_2}{c}) = \sum_{n=-\infty}^{\infty} A_n sinc(\theta_2). \tag{2.32}$$

Using equation 2.30 solve for the unknown coefficient A'_n,

$$A'_n = B\frac{-j\omega\epsilon w_2}{\gamma_n L} cos(\frac{\omega h_2}{c}) sinc(\theta_2). \tag{2.33}$$

The expression determined in Eq. 2.33 may then be plugged directly into Eq. 2.29 to yield,

$$A_n = \frac{j\omega\epsilon D w_1}{\gamma_n L} sin(\frac{\omega h}{c}) \frac{sinc(\theta_1)}{sinh(\gamma_n b)} + \frac{j\omega\epsilon B}{\gamma_n} \frac{w_2}{L} cos(\frac{\omega h_2}{c}) sinc(\theta_2) coth(\gamma_n b). \tag{2.34}$$

Using equations 2.33 and 2.34, the bracket in the RHS of Eq. 2.31 can be expressed in terms of the coefficients of the cavity field (D) and the cathode field (B):

$$A_n cosh(\gamma_n b) + A'_n sinh(\gamma_n b) = \frac{D j\omega\epsilon}{\gamma_n} [\frac{w_1}{L} sin(\frac{\omega h}{c}) sinc(\theta_1) coth(\gamma_n b)] + \frac{j\omega\epsilon B}{\gamma_n} [\frac{w_2}{L} cos(\frac{\omega h_2}{c}) sinc(\theta_2) coth(\gamma_n b) cosh(\gamma_n b) - \frac{w_2}{L} cos(\frac{\omega h_2}{c}) sinc(\theta_2) sinh(\gamma_n b)]. \tag{2.35}$$

Upon using the hyperbolic trigonometric identity ($cosh^2(x) - sinh^2(x) = 1$) for all x, Eq. 2.35 becomes,

$$A_n cosh(\gamma_n b) + A'_n sinh(\gamma_n b) = \frac{D j\omega\epsilon}{\gamma_n} [\frac{w_1}{L} sin(\frac{\omega h}{c}) sinc(\theta_1) coth(\gamma n b)] + \frac{j\omega\epsilon B}{\gamma_n} [\frac{\frac{w_2}{L} cos(\frac{\omega h_2}{c}) sinc(\theta_2)}{sinh(\gamma_n b)}] \tag{2.36}$$

Substituting Eq. (2.36) into Eq.(2.31), we have

(2.37)
$$-\frac{Dcos(\frac{\omega h}{c})}{j\mu c} = \sum_{n=-\infty}^{\infty} \frac{j\omega\epsilon}{\gamma_n}[D\frac{w_1}{L}sin(\frac{\omega h}{c})sinc(\theta_1)coth(\gamma_n b) + B\frac{\frac{w_2}{L}cos(\frac{\omega h_2}{c})sinc(\theta_2)}{sinh(\gamma_n b)}sinc(\theta_1)].$$

Organizing all the terms with the coefficient D to one side and replacing the following relations for the speed of light $c = \frac{1}{\sqrt{\mu_0\epsilon_0}}$, Eq. (2.37) is written as,

(2.38)
$$D * U = B * Y.$$

Providing the same analysis with Eq. (2.28) and using Eqs. (2.33) and (2.34), we obtain another relation between B and D, B*V=-D*Z. This relation, together with Eq. 2.38, leads to the dispersion relation [32],

(2.39)
$$UV = -YZ. \qquad \textit{(Even Modes)}$$

where U,V,Y,Z are;

(2.40a)
$$V = sin(\frac{\omega h_2}{c}) + cos(\frac{\omega h_2}{c}) \sum_{n=-\infty}^{\infty} \frac{\omega}{\gamma_n c}\frac{w_2}{L}sinc^2(\theta_2)coth(\gamma_n b)$$

(2.40b)
$$U = cos(\frac{\omega h}{c}) - sin(\frac{\omega h}{c}) \sum_{n=-\infty}^{\infty} \frac{\omega}{\gamma_n c}\frac{w_1}{L}sinc^2(\theta_1)coth(\gamma_n b)$$

(2.40c)
$$Z = \frac{w_1}{L} \sum_{n=-\infty}^{\infty} \frac{\omega}{\gamma_n c}\frac{sin(\frac{\omega h}{c})}{sinh(\gamma_n b)}sinc(\theta_2)sinc(\theta_1)$$

(2.40d)
$$Y = \frac{w_2}{L} \sum_{n=-\infty}^{\infty} \frac{\omega}{\gamma_n c}\frac{cos(\frac{\omega h_2}{c})}{sinh(\gamma_n b)}sinc(\theta_2)sinc(\theta_1)$$

(2.40e)

The odd-mode solutions are found in a similar manner but require that the boundary condition along the horizontal line of symmetry at $x = -h_2$ where the electric

field will go to zero. The form of the odd mode field equations, within the cathode (region-II), then has a similar form as the cavity fields (region-III). The resultant solutions are expressed in a similar manner to the even-modes where [32]:

$$U'V' = Y'Z'. \qquad \textit{(Odd Modes)} \tag{2.41}$$

$$V' = cos(\frac{\omega h_2}{c}) - sin(\frac{\omega h_2}{c}) \sum_{n=-\infty}^{\infty} \frac{\omega}{\gamma_n c} \frac{w_2}{L} sinc^2(\theta_2) coth(\gamma_n b) \tag{2.42a}$$

$$U' = cos(\frac{\omega h}{c}) - sin(\frac{\omega h}{c}) \sum_{n=-\infty}^{\infty} \frac{\omega}{\gamma_n c} \frac{w_1}{L} sinc^2(\theta_1) coth(\gamma_n b) \tag{2.42b}$$

$$Z' = \frac{w_1}{L} \sum_{n=-\infty}^{\infty} \frac{\omega}{\gamma_n c} \frac{sin(\frac{\omega h}{c})}{sinh(\gamma_n b)} sinc(\theta_2) sinc(\theta_1) \tag{2.42c}$$

$$Y' = \frac{w_2}{L} \sum_{n=-\infty}^{\infty} \frac{\omega}{\gamma_n c} \frac{sin(\frac{\omega h_2}{c})}{sinh(\gamma_n b)} sinc(\theta_2) sinc(\theta_1) \tag{2.42d}$$

(2.42e)

When w_2 approaches zero, the geometry reduces to a solid cathode with a perfectly conductive boundary along $x = 0$. The expression for Y, in Eq. 2.40d, will tend to zero with w_2 and, since V is still a finite value in this limit, the term U must go to zero in Eq. 2.39. Setting the RHS of (U) to zero in Eq. (2.40b) yields the expression for a simple planar cavity array found in many textbooks,

$$cot(\frac{\omega h}{c}) = \sum_{n=-\infty}^{\infty} \frac{\omega}{\gamma_n c} (\frac{w_1}{L} sinc^2(\theta_1) coth(\gamma_n b)). \tag{2.43}$$

Some numerical examples from the dispersion relations, Eq. 2.39 and Eq 2.41, will be shown in the next chapter.

2.1.3 Planar Magnetron Operation

A well-tuned magnetron that is operating within a synchronous state between the drifting electron beam and the RF wave will develop perturbations to the nominal

laminar flow model depicted in Fig.2.2B [49]. These perturbations augment during operation primarily due to the existence of the periodic $\vec{E_{RF}}X\vec{B}$ noted in Fig. 2.3 as well as a "self-focusing" effect, inherent to π-mode operation, to form well defined structures referred to as electron "spokes" [50]. Qualitatively, magnetron self focusing can be described using the same single particle argument in Fig. 2.3, assuming there are two or more particles, one lagging and the other leading the "green" electron. It is easy to see that the vertical RF electric field would bring these two neighboring electrons to the "green" electron, where the spoke is found. The sharpening of the spoke structure by this phase focusing mechanism is shown in Fig. 2.7.

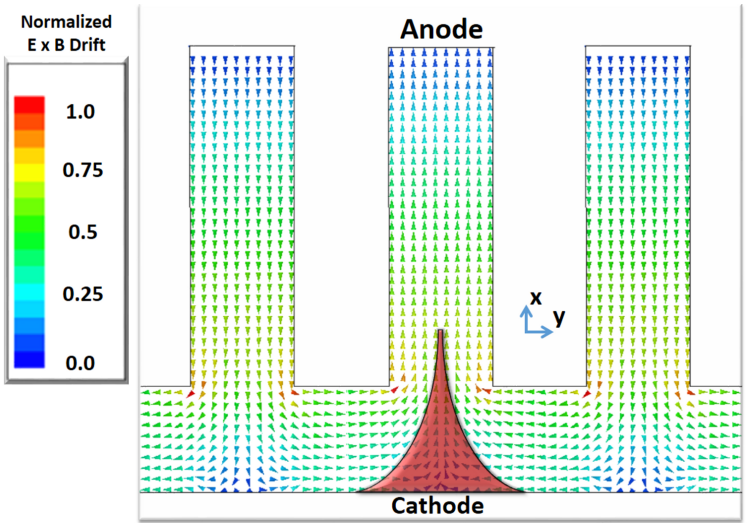

Figure 2.7. Sample section of the RPM slow wave structure and solid cathode with arrows represent the direction and normalized magnitude and direction of the $\vec{E_{RF}}X\vec{B}$ drift experienced by the particles as well as the spoke formation caused by these drifts (shaded red).

Self-focusing in the modified MCC geometry introduces the potential benefit of additional communication between the two oscillators of the RPM. The even π-mode, for which the fields are in phase between top and bottom oscillator, produce a mono-directional $\vec{E}X\vec{B}$ drift, shown in Fig. 2.8. The induced $\vec{E_{RF}}X\vec{B}$ drift incorporates the RF field from cavities on either oscillator which greatly enhances the transport

of RF and electrons between each side of the device. The self-focusing effect in each pair of cavities, one in the top oscillator and one in the bottom oscillator, for the even π-mode of the MCC is anticipated to vastly improve the potential for phase-locking between the two slow-wave structures, generate faster startup, and improve mode stability.

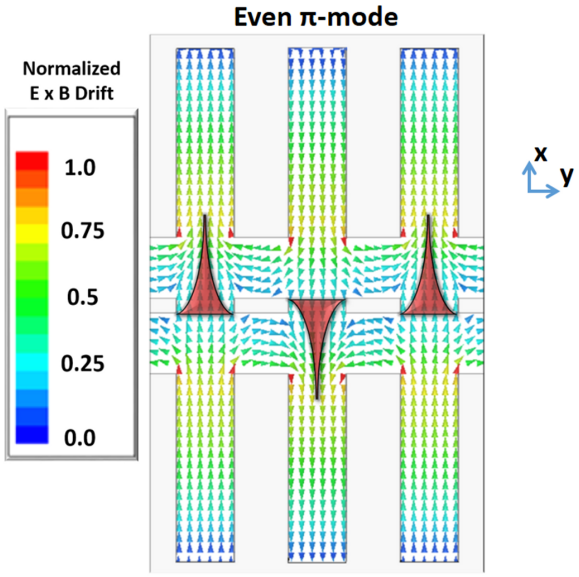

Figure 2.8. Sample section of the RPM slow wave structure and MCC with arrows represent the normalized magnitude and direction of the $\vec{E_{RF}} X \vec{B}$ drift experienced by the particles as well as the spoke formation caused by these drifts (shaded red).

The net result of electronic self focusing in a magnetron is a higher than nominal electron population in regions of phase-space that will give energy to the RF wave (like the "green" electron in Fig. 2.3) and a lower electron density in the regions that will be accelerated by the RF (like the "red" electron in Fig. 2.3). This intrinsic feature of the magnetron, coupled with the favorable energy transfer mechanism mentioned previously, permit the magnetron to operate with very high efficiency [2]. A qualitative visualization of RPM operation is given in Fig. 2.9(A-D), which de-

picts four stages of mode development corresponding to different points in time. Fig. 2.9A shows the initial emission of electrons into the AK-gap of the diode, these particles experience little influence from surrounding space-charge and largely undergo unperturbed cycloidal orbits. Later in time, Fig. 2.9B, the collective motion of the electrons forms a hub with a laminar velocity profile, as predicted in Brillouin flow models [49]. Broadband noise within the hub then excites the resonant cavities which begin to build up RF power over several cycles illustrated by Fig. 2.9C. Once the stored RF power reaches a sufficient magnitude, the influence of the E_{RF} field begins to perturb the laminar hub, initiating the formation of electron spokes as shown by Fig. 2.9D. The self-focusing effects readily augment and saturate into a steady operating state of the magnetron.

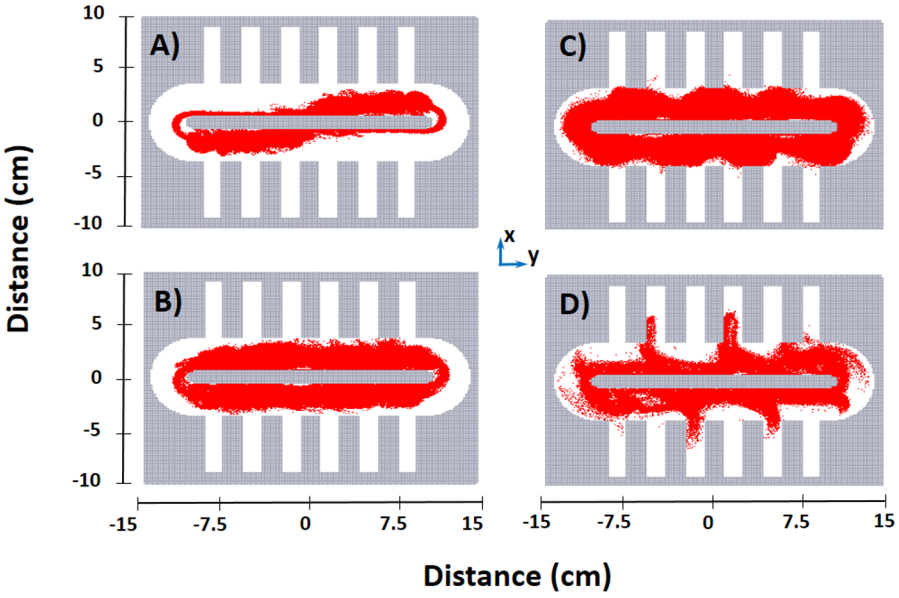

Figure 2.9. Simulated magnetron operation (in MAGIC PIC) of the RPM-12a with solid cathode for varying stages of mode development including: A) Initial electron emission (19 ns), B) Brillouin flow and electron hub formation (24 ns), C) RF perturbations on laminar flow (43 ns), and D) Full π-mode operation (60 ns).

CHAPTER III

Simulation and Design of the Recirculating Planar Magnetron

3.1 Design of the RPM-12a

The initial study of the RPM was performed using the analytic resonance and synchronism conditions, described in Chapter 2, in conjunction with the particle-in-cell (PIC) code, MAGIC [51]. The goal of this design phase was to establish an RPM anode configuration that could readily operate using experimentally viable fields of -250 to -300 kV and 0.15 to 0.2 T axial magnetic fields, as well as satisfy the geometric constraints of the 39.4 cm ID vacuum chamber.

Numerous 2D simulations were generated in MAGIC PIC using these analytic and physical criteria and were then evaluated on the basis of operating frequency, mode separation, and beam velocity. An example 1 GHz, 20 cavity, RPM simulation performed in MAGIC is shown in Fig. 3.1.

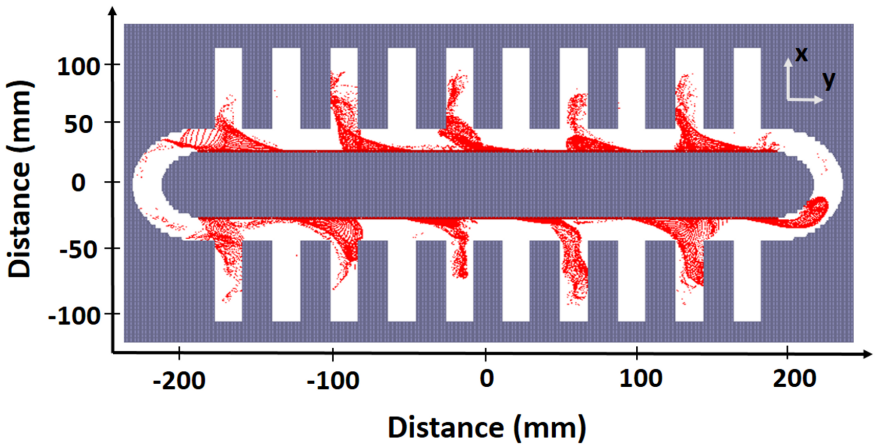

Figure 3.1. 2D Simulation in MAGIC PIC of the initial L-band RPM-prototype. External magnetic field points out of the paper.

This particular model had a 2 cm AK gap and operated in π-mode using a -300 kV applied voltage and 0.16T axial magnetic field. The depth of the resonant cavities was found, analytically, to be 6.31 cm in order to attain a cold π-mode resonance at 1.007 GHz and a 2D beam loaded resonance at 1 GHz. The length of the vanes and cavities (in the $\hat{y}$ direction), for simplicity, were made equal at 1.92 cm, which provides a slow wave structure period (L) of 3.84 cm and a π-mode guided wavelength of 7.86 cm. The corresponding phase velocity where, $v_\phi = 2Lf_0$, is therefore 0.26 c. The radius of the anode, or outer radius of curvature in the cylindrical bend, was set at 4.5 cm in order to maintain an estimated electric beam velocity between 0.25 c and 0.3 c [31]. Initial designs in both MAGIC PIC and experiment utilized a 2 cm AK gap with a 5 cm-thick hollow copper cathode; designated as Solid Cathode-1 (SC-1). Later designs for the solid cathode reduced the thickness of the the electrode in favor of smaller, lighter, geometry in order to reduce parasitic current emission and increase the AK gap to mitigate the effects of diode gap closure. The smaller

cathode denoted as the Low Current-1 (LC-1) model had a thickness of 1.28 cm and produced an AK gap of 3.87 cm. Using this model as a template, A 12-cavity model (RPM-12a) was chosen (6 cavity-vane pairs on either planar side) to balance mode competition with peak power [3] as well as match the spatial restrictions of the experimental environment. The RPM-12a design was extrapolated into 3D MAGIC PIC simulations and the anode block was designed to inhibit the development of axial modes by limiting the axial length to 11 cm, well below half of the free space wavelength (15 cm). A 3D visualization of the RPM-12a is shown in Fig. 3.2.

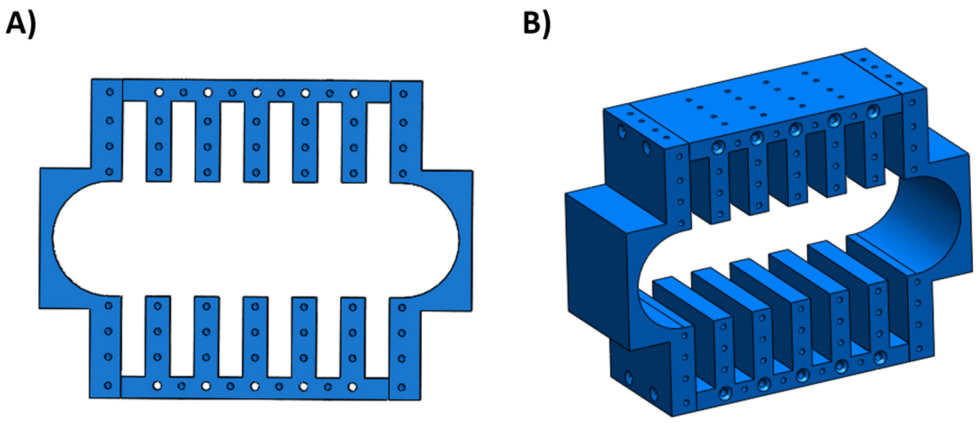

Figure 3.2. 3D rendering of the RPM-12a in SolidWorks from front-on perspective (left) and oblique-perspective (right).

3.1.1 Numerical Cold Tests: Solid Cathode

The RPM-12a structure is most easily analyzed by using a single period, the most fundamental structural component, Fig 3.3. The single period can be modeled to exactly reflect the simplified geometry used in the analytic dispersion derivation by

using master-slave boundary conditions to replicate an infinite planar cavity array shown in Fig. 2.5.

Using the Eigenmode solution routine in finite element program, High Frequency Structure Simulator (HFSS) [52], specific resonance modes of the RPM can be identified by setting a discrete phase shift between the master boundary and the slave boundary. This phase shift per cavity ($\delta\phi$), in degrees, is related to the planar propagation constant (β_0) by the following relation,

$$\beta_0 = \frac{2\pi}{\lambda_g} = \frac{2\pi(\delta\phi)}{360L}. \tag{3.1}$$

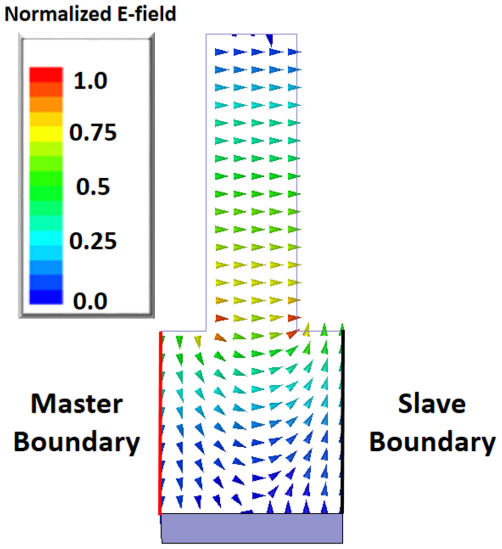

Figure 3.3. Infinite, planar cavity array for the solid cathode geometry represented by a single periodic structure with master/slave boundary conditions in HFSS.

The fundamental modes of the cold tube dispersion relation can be found by sweeping the phase shift per cavity from 0 to 360 degrees. The simplification of the 2D slow-wave structure does induce some errors, as the model no longer accounts for both the finite length of the planar slow wave structure and the fringing RF electric and magnetic fields entering the chamber on either axial end of the anode. These geometric discrepancies are fully addressed using a full 3D model of the device, with surrounding vacuum chamber, in HFSS. Perfectly Matched Loads (PMLs) are included on either axial end of the chamber to both establish a more realistic quality factor (Q) and inhibit the solver from identifying chamber RF resonant mode structures as opposed to the desired RPM mode. Additionally, the fully 3D model includes the cylindrical bends which couple the two planar slow-wave structures. The inclusion of this weak coupling mechanism will create the bifurcated mode structure that is a natural product of the RPM geometry as described in Chapter 2. The resulting resonant mode structure includes both even and odd spatial degeneracies for each individual mode defined by a given phase shift per cavity. The modes shown in Fig. 3.4 are visual representations of the fully 3D even and odd -modes and $5\pi/6$ modes for the RPM 12a.

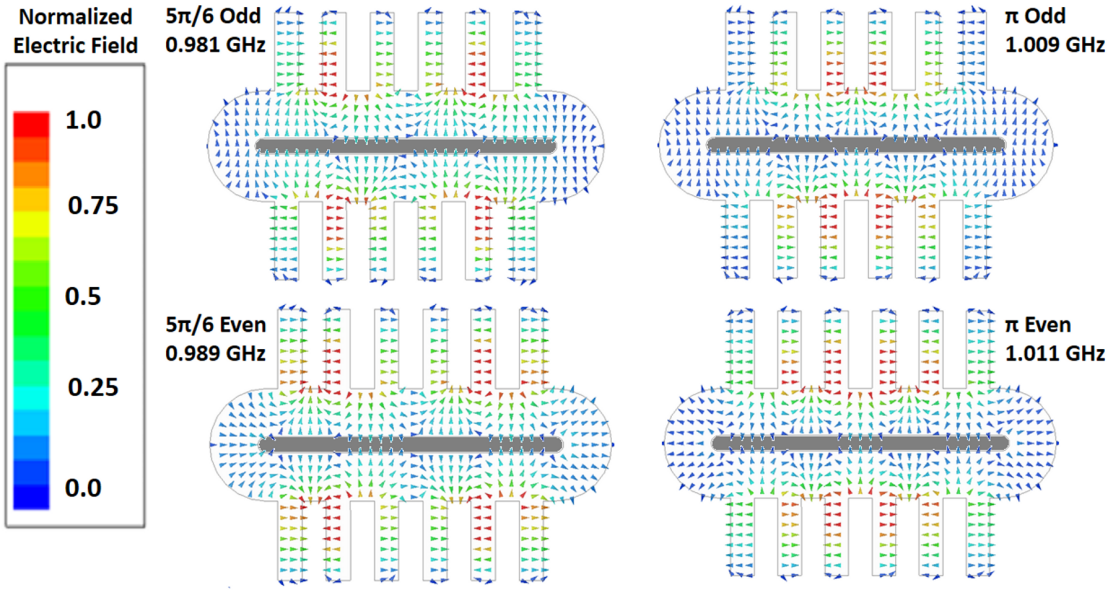

Figure 3.4. Electric field configurations for the even and odd $\frac{5\pi}{6}$-modes (left) and π-modes (right) found using HFSS.

A comparison of the dispersion relation. Eq. 2.43, generated by the two models is shown in Fig. 3.5. The dispersion relation in Fig. 3.5 demonstrates excellent agreement between the 2-D HFSS model and the analytic model, Eq. 2.43.

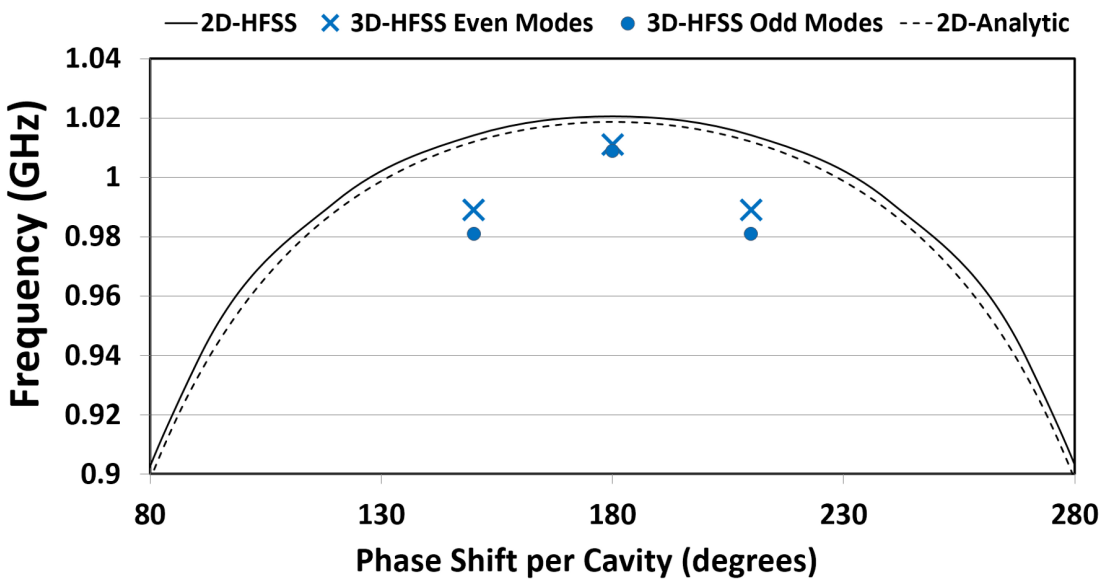

Figure 3.5. Dispersion relation for the even modes of the RPM-12a as found using the analytic model (dashed-black), an infinite planar array in HFSS (black) and a finite 12 cavity geometry with fringe fields (blue X's).

The 3D model is more accurate than either 2D representation, but much more taxing computationally, identified π-mode at 1.011 GHz, deviating only 7 MHz or 0.0068 % from the analytic estimate. Neighboring degeneracies of $5\pi/6$ and $7\pi/6$ displayed a much larger discrepancy of nearly 23 MHz between analytic and 3D representation. This result also implies that 3D effects yield much larger separation between the π-mode and neighboring modes ($5\pi/6$ and $7\pi/6$). The analytic model appears to be very capable of identifying the relative operational position of π-mode due predominantly to the periodic symmetry of electromagnetic fields in the finite structure. Electromagnetic field configurations that deviate from this perfect periodic symmetry, such as the $5\pi/6$, will experience drastically difference boundary conditions between a structure with a finite number of cavities and an infinite planar array.

3.1.2 Numerical Cold Tests: Mode Control Cathode

The modified dispersion relation including the MCC may also be analyzed using the 2D periodic representation in HFSS. Since the MCC incorporates coupling between the two oscillators within the single period geometry, the 2D model is more accurately modeled using a single cavity of both the top and bottom oscillator as seen in Fig. 3.6.

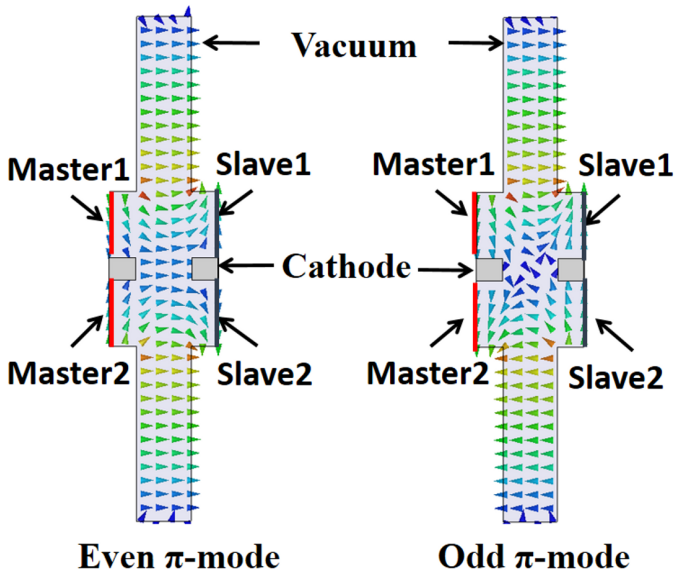

Figure 3.6. Infinite planar cavity array for the MCC geometry represented by a single unit of the structure with master/slave boundary conditions in HFSS.

The geometry in Fig. 3.6 is a proof-of-principle configuration which features a cavity length (h) of 6.3 cm, an AK gap (b) of 2 cm, a 1.92 cm cavity width (w_1), and 1 cm cathode width (h_2) was used to both reflect the RPM-12a anode geometry with MCC and for the analytic simplicity of Fig. 2.6. The modified dispersion relation, which is analyticalyl described in Eqs. 2.39 and Eq. 2.41, was solved for both numerically and in simulation using the 2D, infinite planar array, model and compared in Fig.

3.7.

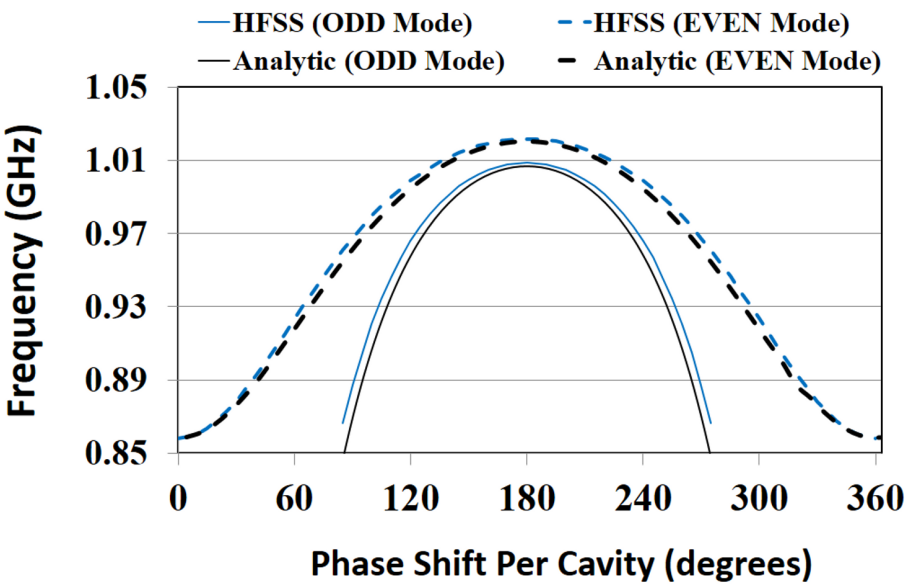

Figure 3.7. Dispersion relation including the mode control cathode for the even (dashed-black) and odd (black) modes using the analytic model compared to the even (dashed-blue) and odd (blue) modes in the infinite cavity array in HFSS.

The separation between even and odd modes is at a minimum at 180 degree phase shift per cavity, or π-mode, and increases as the mode number is increased or decreased. Additional separation between neighboring modes can be attained by adjusting the mode control cathode geometry which is shown for (even-odd) π-modes in Fig. 3.8 using parameter sweep of the cathode height (h_2), cathode width (w_2), and AK gap (b) [32].

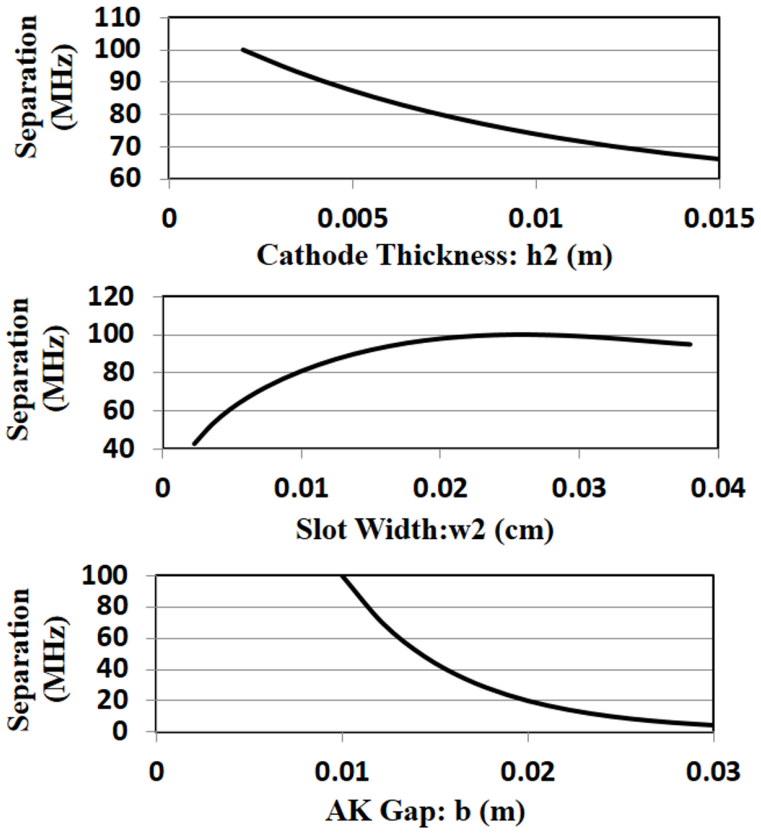

Figure 3.8. Analytic mode separation results between the even and odd pi-modes for: A) varying parameter (h2) and setting w2=0.024 m, AK=0.01 m, B) varying parameter (w2) and setting h2=0.002 m, AK=0.01 m, and C) varying parameter (b) and setting w2=0.024 m, h2=0.002 m.

Mode separation between the even and odd π-mode, in the RPM-12a slow wave structure with MCC, is maximized as the AK gap approaches zero. Under realistic parameters (AK gap $>$ 1cm) even-odd mode separation can theoretically reach 100 MHz, but this separation is reduced as the AK gap is increased past 1 cm. Long-pulse relativistic devices typically require larger AK-gaps due to plasma expansion from the cathode and subsequent gap closure in the diode; this may limit pulse duration or mode separation. Mode separation asymptotically approaches zero after the AK gap exceeds 3 cm. The study of the MCC is focused on two primary geometries designated as MCC-1, designed to produce an effective AK gap similar to that of the

LC-1, and the MCC-2 which results in an AK gap of approximately 2 cm, for which the RPM was originally designed.

Cathode Design: MCC-1

The MCC-1 is composed of 5 cylinders (used to reduced edge sharpness of a rectangular-shape cathode), each with a diameter of 2.22 cm, forming an AK gap 3.38 cm; from Fig. 3.8C, this will limit the even and odd separation. Instead, the cathode is utilized almost entirely as an emission-primed electromagnetic coupler, designed to increase the potential of phase locking the RPM oscillators. Each conductive cylinder is spaced 3.84 cm apart to match the vane-cavity periodicity of the RPM-12a and is bounded by cylindrical end-loss inhibitors on either axial end of the device. This initial design features rounded components to reduce field enhancement on the edges of the device and limit current emission from undesired locations [11, 53]. The dispersion relation for the MCC-1 is compared to the solid cathode (LC-1) using 2D models in Fig. 3.9.

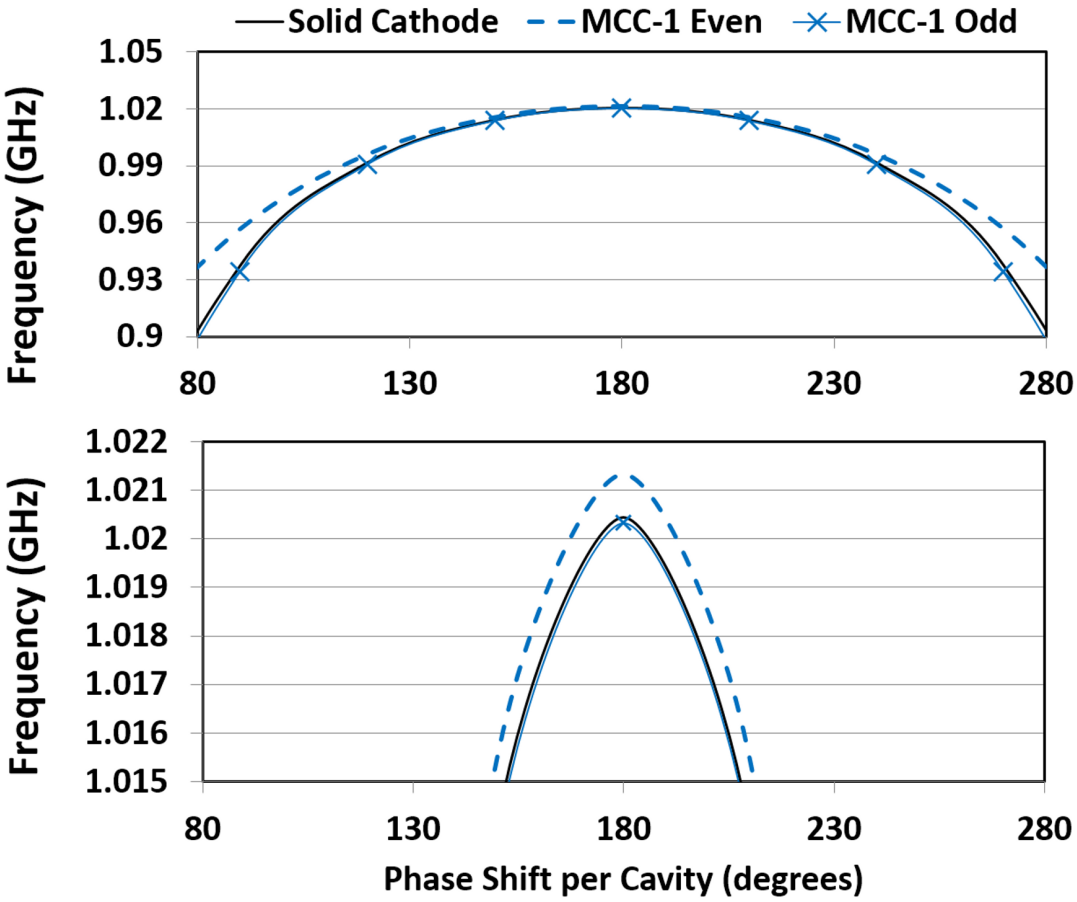

Figure 3.9. Dispersion relation for: A) the RPM-12a using a solid cathode (black), as well as the even (dashed blue) and odd (x-blue) modes using the MCC-1 geometry, and B) a zoomed-in illustration of π-mode separation between the even and odd mode solutions.

The MCC-1 was designed entirely to provide cross-oscillator communication and, due primarily to the large AK gap, generates little more than 1 MHz additional separation as compared to the solid cathode. The odd modes, which correspond to a null RF electric field along the horizontal plane of symmetry, have an electric field configuration that is very similar to that of the solid cathode and, as a result, have essentially identical dispersion relation, illustrated in Fig. 3.9B. Thus, locking of the odd π-mode by the MCC is less prominent than the even π-mode.

Cathode Design: MCC-2

The MCC-2 is a larger cathode design that is composed five rectangular conductors that are 1.9 cm ($w_2 = 1.9$ cm) wide by 3.8 cm tall ($h_2 = 1.9$ cm). The MCC-2 was designed to create a smaller AK-gap of ~ 2.6 cm, closer to that of the original simulated design parameter. Each rectangular conductor was spaced 3.84 cm apart to reside directly underneath the vanes of the RPM-12a in the same manner as the MCC-1. The dispersion relation for the MCC-2 is again compared to the solid cathode (LC-1) using 2D models in Fig. 3.10.

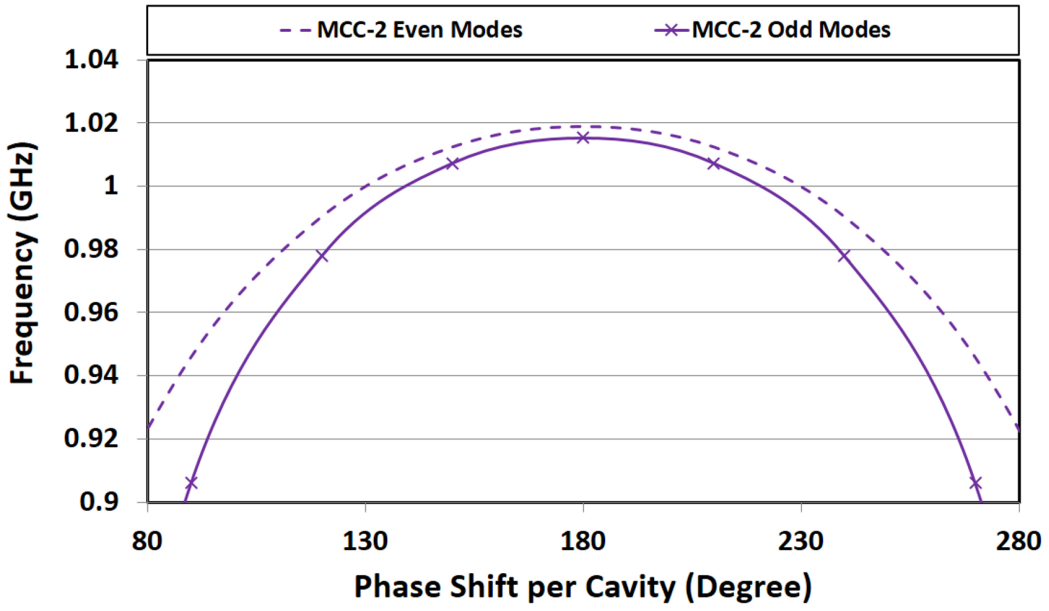

Figure 3.10. Dispersion relation for the RPM-12a using the MCC-2 with the even (dashed purple) modes and odd (x-purple) modes.

Decreasing the separation of the anode and cathode slightly reduces the RF circuit impedance of AK gap which results in a decreased resonant frequency for each mode of the dispersion relation. The MCC-2 demonstrates a modest increase of 4 MHz

separation between even and odd π-modes but is restricted by the large 3.8 cm thickness of the cathode ($2h_2$) which, according to Fig. 3.8A, also restricts the achievable separation between even and odd π-modes.

3.1.3 Electromagnetic Particle in Cell Modeling: Solid Cathode

A 3D model of the full experimental setup for RPM-12a with solid (LC-1) cathode, visually rendered in Fig. 3.11 using Solidworks [54], was simulated using the electromagnetic particle in cell code MAGIC. A -300 kV voltage pulse was imposed on the cathode stalk and the magnetic field was varied between 0.1 and 0.16 Tesla, in order to produce electron beam drift velocities in the vicinity of π-mode phase velocities ($v_{ph} \sim 0.26$ c), for durations of 200 ns.

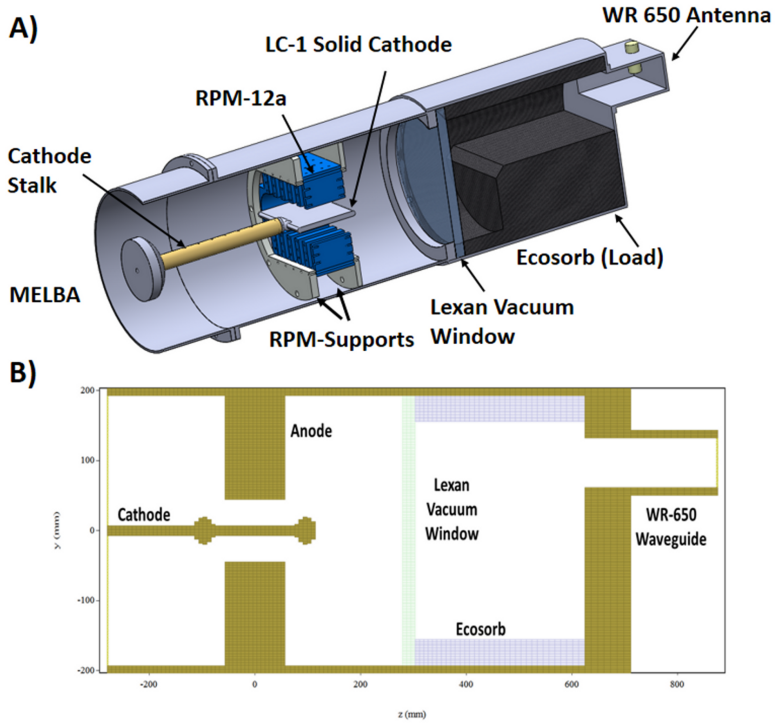

Figure 3.11. A) An oblique 3D rendering of the RPM-12a simulated/experimental configuration made in Solidworks, and B) longitudinal (YZ) cross section of the simulated geometry in MAGIC PIC.

Predictably, in the more realistic environment simulated in MAGIC PIC, there exists a distribution of electrons which violate the ideal rectilinear shear flow model described using Brillouin flow theory in Chapter 2. In these simulations, particles steaming both faster than the synchronous RF circuit phase velocity, as well as, particles that approach a drift velocity of zero above the cathode (a virtual cathode (VC) at point B in Fig. 3.12) are observed once the electron hub has formed. The net result of this phenomenon is a reduced, effective-AK gap (distance from anode to VC), which impacts the applied fields required to achieve synchronism as compared to the physical AK gap (presented as (b) in Fig. 2.6). The position of the VC layer is visually presented by plotting average electron velocity in the $\hat{y}$ direction as a function of position in $\hat{x}$ for all particles in the planar regimes of the RPM 10 ns prior to the development of oscillations.

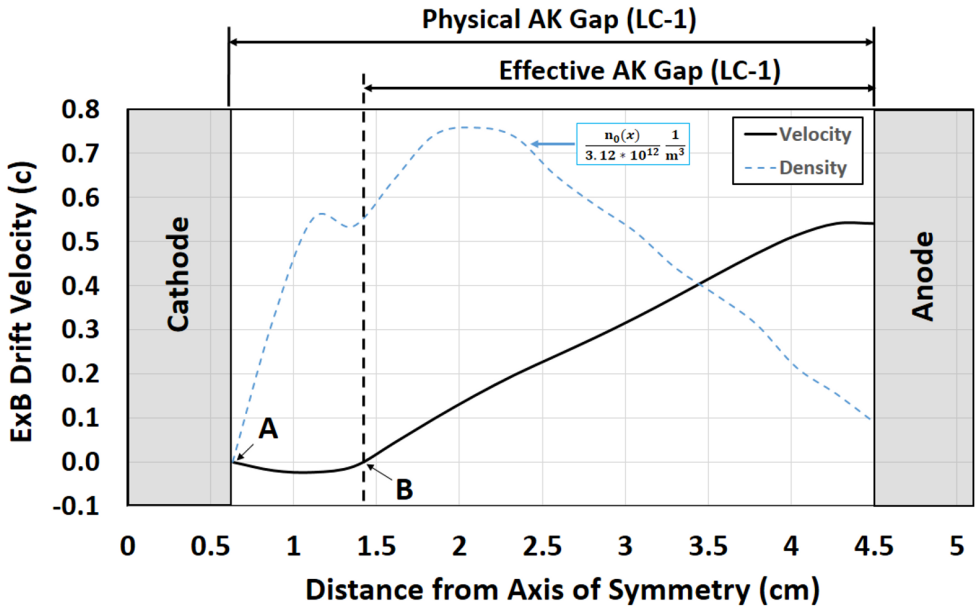

Figure 3.12. Velocity Profile of the the RPM-12a with LC-1 Cathode 10 ns prior to mode-startup as a function of (x), the distance from the horizontal axis of symmetry of the device, with specific emphasis on: A) the start of the Cathode, and B) The Virtual Cathode layer.

Simulations with an applied B field between 0.1 and 0.16 T were run with an applied voltage which was increased from -250 kV to -400 kV until pi-mode oscillations were observed at the even-π-mode frequency at 1.005 GHz for a static magnetic field. The resultant fields required for π mode operation can be compared to the analytic models using Brillouin flow theory described in Chapter 2 [20]. Fig. 3.13 predicts the applied voltage as a function of axial magnetic field for Hull cutoff (black), $5\pi/6$-mode (grey) and π-mode (blue) for the physical AK gap (3.88 cm), as well as π-mode for the adjusted AK-gap (3.16 cm) due to the virtual cathode effect (blue dashed).

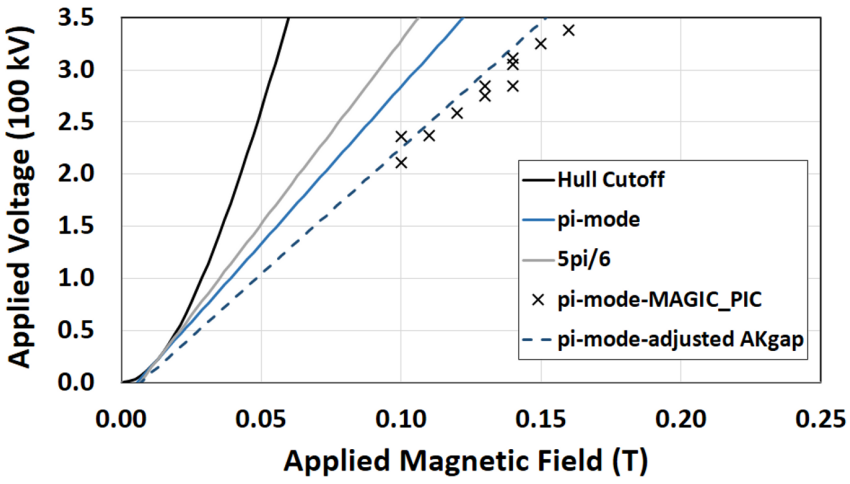

Figure 3.13. Applied voltage as a function of axial magnetic field required to reach Hull Cutoff (black), $5\pi/6$-mode (grey), π-mode (blue), and π mode with adjusted AK-gap due to virtual cathode (dashed-blue) for the RPM-12a with LC-1.

3.1.4 Electromagnetic Particle in Cell Modeling: Mode Control Cathode

Fundamental PIC analysis of this MCC is performed by simulating a 2 D model of the RPM-12a equipped with the proof-of-principle geometry described in Table 3.1 and Fig. 2.6.

Table 3.1. Proof of Principle Mode Control Cathode dimensions.

Parameter	**Dimension**
b	2.4 cm
w_1	1.9 cm
w_2	1.9 cm
h	6.3 cm
h_2	0.5 cm

Re-entrant boundary conditions are imposed on either end of a 6-cavity model shown in Fig 3.14, in order to isolate the coupling effects provided by the cathode itself from that of the cylindrical recirculation regions [27]. Each simulation used an applied voltage of -300 kV for 300 ns on either a solid conducting cathode (Fig. 3.14A), to isolate the two sides, or the MCC (Fig. 3.14B-C) with a slotted geometry. The presence of cross-oscillator coupling is shown in these simulations to enhance stability as local perturbations imposed on one side of the device can be readily corrected by stable operation of the other side and vice versa. The degree of cross-oscillator communication is a function of the MCC geometry, which can be easily manipulated to tune the magnitude of RF power propagating through the slotted gaps. RF power coupling, between the oscillators of the RPM, of a sufficient magnitude and temporal length will induce a state of locked operation wherein the relative phase difference of symmetric cavities on either side of the RPM will be constant. The RPM with MCC features two identical strongly-coupled oscillators and behaves in a manner similar to the "Peer to Peer" configurations described by Woo et al [55].

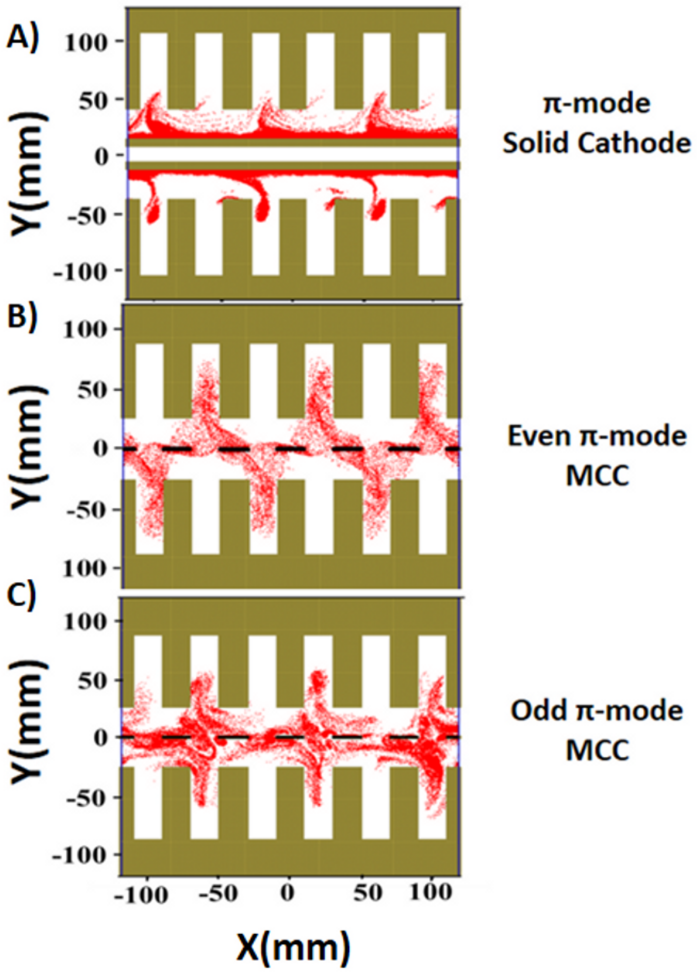

Figure 3.14. 2D MAGIC PIC image of a dual reentrant magnetron operating in: A) π-mode using a solid cathode, B) even π-mode using a MCC, and C) odd π-mode using a MCC.

A phase locking study was performed using this simulated model by sweeping the AK gap [b in Table 3.1 and Fig. 2.6] from 1.0 cm to 3.2 cm in order to alter the magnitude of the transverse electric field (E_y) at the cathode. The two oscillators are considered to have achieved a locked state when the relative phase between two symmetric cavities on the top and bottom does not vary more than $\pm$ 2 degrees for 50+ ns [55–57]. Simulations were modeled using a 0.18 T uniform axial magnetic field (B) for 300 ns and the applied voltage (V) was varied to scale the electric field

as dictated by Bunemann-Hartree condition for the even π-mode in a planar diode (-150kV to -500kV). Both oscillation start-up times and phase-locking times were monitored for each simulated case and are illustrated in Fig. 3.15.

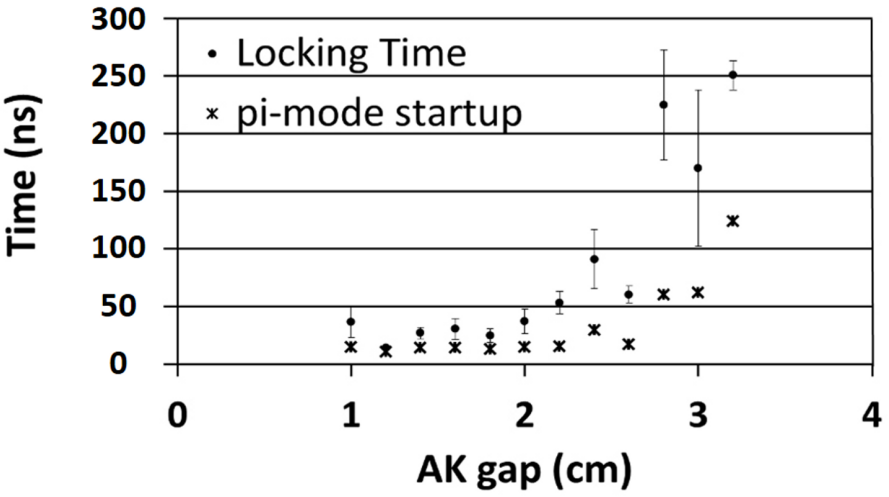

Figure 3.15. Simulated results of the simulated "reentrant planar magnetron" with MCC showing oscillation start up times (x) and phase locking times (dots) as a function of the AK gap.

The simulated control case depicted by (Fig. 3.14A), with a solid aluminum cathode and 2.4 cm AK gap, demonstrated π-mode oscillations after approximately 100 ns but, due to the complete isolation between oscillators, was incapable of achieving phase-locked operation. The MCC produced even π-mode oscillations in less than 30 ns under the same operating conditions and reached a phase-locked state between opposing slow wave structure in less than 100 ns.

Cathode Hot Test: MCC-1

The "rounded" MCC-1 was evaluated using the same simulated model as described in Fig. 3.11 operating with a -200 to -300 kV pulsed voltage with applied magnetic fields between 0.08 and 0.2 T for durations of 200 ns. The RPM-12a with

MCC-1 anode-cathode geometry is shown operating in π mode in Fig. 3.16.

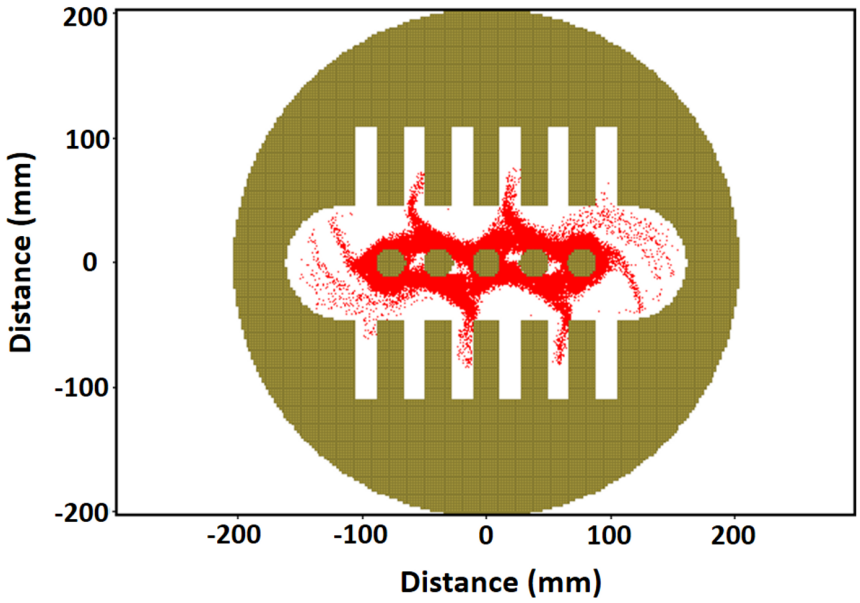

Figure 3.16. A transverse cross section (XY) phase-space particle plot depicting even π-mode operation of the RPM-12a using the MCC-1 in MAGIC PIC.

Similar to the solid cathode (LC-1), a virtual cathode effect develops within the device. The space between the conductors of the MCC, however, allows for the electron hub to develop closer to the axis of symmetry rather than the outer most conductive surface. As a result, the VC layer is formed closer to the actual cathode surface (as compared to the RPM-12a with LC-1 cathode in Fig. 3.12) where the effective AK gap and the physical AK gap are nearly equal. Figure 3.17 shows the simulated average velocity in the $\hat{y}$ direction as a function of position in $\hat{x}$ for all particles in the planar regime of the RPM-12a with MCC-1.

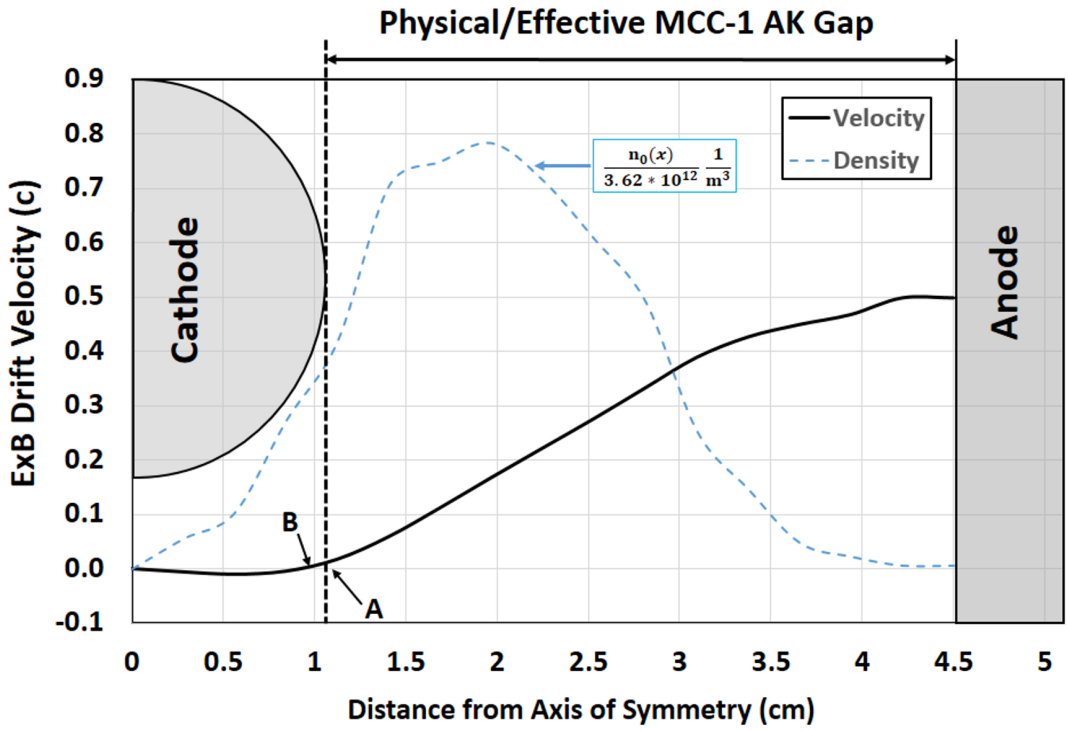

Figure 3.17. Velocity Profile of the the RPM-12a with MCC-1 Cathode 10 ns prior to mode-startup as a function of (x), the distance from the horizontal axis of symmetry of the device, with specific emphasis on: A) the start of the Cathode, and B) The Virtual Cathode layer.

A comparison between the theoretical and simulated applied fields, required for π-mode operation of the RPM-12a with MCC-1, is made in Fig. 3.18. In this figure, the simulated voltages and magnetic fields, observed in MAGIC PIC, are overlaid on the theoretical Buneman-Hartree curves for this geometry. The AK gap for the theoretical Buneman-Hartree curves is measured from the outer-most surface of the cathode to the anode.

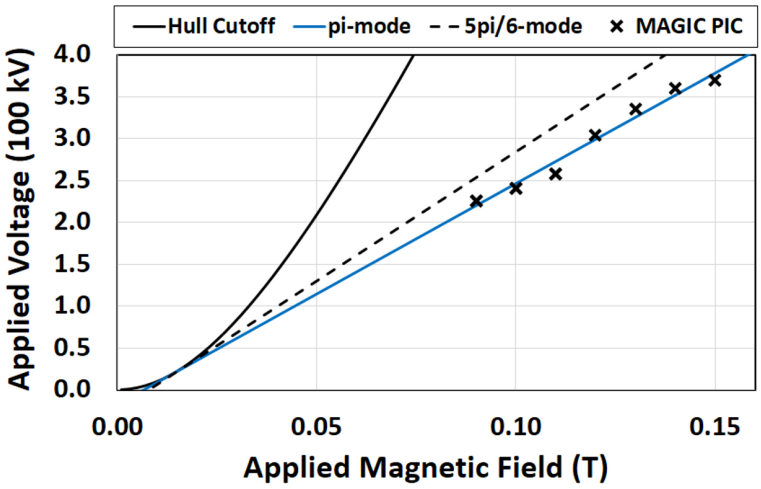

Figure 3.18. Analytic Hull cutoff (black) and Buneman Hartree curves for $\frac{5\pi}{6}$ (dashed) and π (blue) modes overlaid with the applied potential and magnetic field for even π-mode startup of the RPM-12a with rounded MCC-1 (X) in MAGIC PIC.

The simulated results of the MCC-1 in MAGIC PIC show excellent agreement to the planar theory described in Chapter 2 both in the resonant frequency of the even π-mode (1.005 GHz) and the applied fields required to achieve synchronism. The MCC-1 achieved phase locking within $\pm$ 10 degrees approximately 55 ns after startup with an applied magnetic field of 0.12 T and after 75 ns when operating with 0.14 T field.

The RPM-12a with the thicker MCC-2, shown operating in π-mode in Fig. 3.19, displayed minimal circulation of the electron beam through the cathode suggesting that the $\vec{E}X\vec{B}$ drift due to the fields between the cathode arrays was much smaller than the $\vec{E}X\vec{B}$ drift experienced in the AK gap.

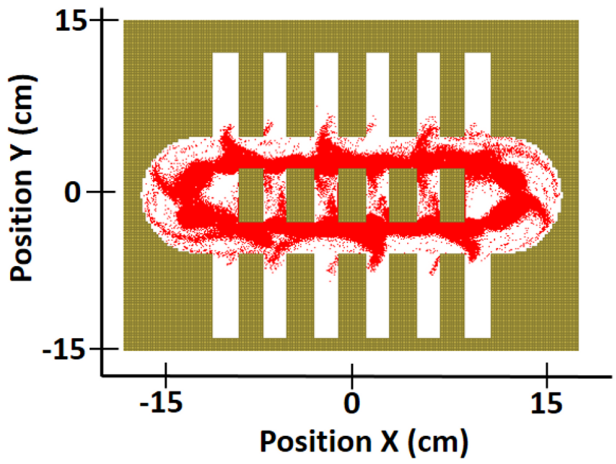

Figure 3.19. A transverse cross section (XY) phase-space particle plot depicting even π-mode operation of the RPM-12a using the MCC-2 in MAGIC PIC.

The MCC-2 operated in even-π mode at 1.00 GHz using a -300 kV applied voltage and 0.15 T axial magnetic field. The smaller AK gap enabled the RPM-12a to startup after 50 ns and achieve a state of locked operation after only 35 ns post-startup. The MCC-2 when operating in the odd-π mode, with a 0.14 T magnetic field and -270 kV applied voltage, operated at 0.995 GHz and did not achieve a locked-state of operation until 48 ns post-startup.

3.2 Extraction Concepts and Design

Extraction for the RPM was conducted as a two-stage project, consisting of a Proof of Principle (PoP) coaxial extractor and the Coaxial All Cavity Extractor (CACE). Extraction designs for the RPM were guided heavily by the existing experimental setup which dictated the use of an axially oriented scheme that could easily reach the forward port of the cylindrical vacuum chamber. The transmission-network forming both the PoP and CACE were designed to both fit within the 34.3 cm diameter of the forward chamber vacuum port and maintain the capacity to handle 10s to

100s of MWs produced by the RF generator. Additional infrastructure is included axially downstream from the coaxial transmission lines (CTL) to convert the signals to an easily diagnosed TE_{10} mode.

3.2.1 Coaxial to Waveguide Coupler Design

Conversion of the RF power from a coaxial transmission line into a rectangular waveguide is highly advantageous for diagnosis in a laboratory setting and antennas as CTLs may adversely respond to perturbations such as bends or coupling slots. The additional conversion, however, is not easily accomplished due to proximity of adjacent extractors. Orthogonal, high power, couplers such as door knobs [58] or inductive/capacitive antenna couplers are classically implemented in a manner that requires H-plane orientation of the waveguide [59]. This orientation creates a spatial restriction requiring high RF phase velocities or unphysical overlap between transmission lines. We instead utilize an in-line or magnetic field mode converter which, if properly designed, may seamlessly transition from a CTL to waveguide without increasing the nominal cross sectional area of the extractor [60]. A novel device designed to address this in-line conversion for pulsed high power environments is the distributed field adapter (DFA).

The DFA is designed to alleviate electric field enhancement on the surface of the coupler by providing a process for mode conversion that maximizes the distribution of axial Poynting flux over a broad, smooth, purely conductive surface. This distribution of power is achieved by elongating the conductive structures of magnetic coupling loop in order to extend the transitional TE_{11} mode in the axial direction. The surface area of these coupling structures are then maximized using rounded surfaces (cylinders and ellipses) to achieve a minimal Poynting flux density in the coupler region. The increased length of the mode conversion process allows for the

DFA to be designed as a high impedance transformer to operate at frequencies approaching the TE_{10} cutoff [61].

The DFA is presented in three embodiments in Fig. 3.20 (A-C) which characterize a natural trade-off between power handling and structural complexity. The DFA, as shown, uses an adaptation of a two-step staircase impedance transformer, additional stages can be used to increase bandwidth at the cost of complexity both in design and fabrication.

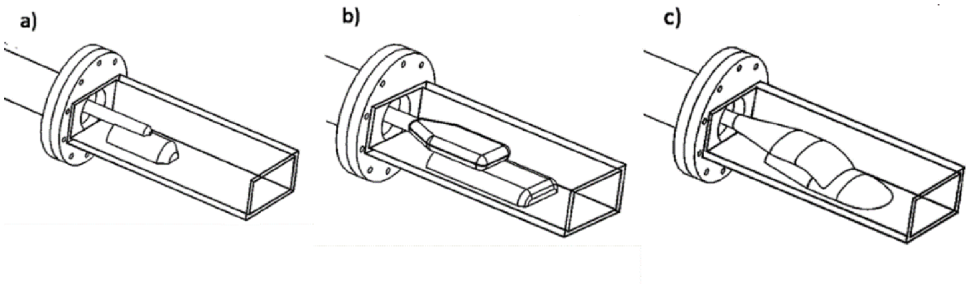

Figure 3.20. A) The cylindrical cross section DFA, B) the rounded rectangular cross section DFA, and C) the elliptical cross section DFA.

Two prototypes were designed from these embodiments including an L-band cylindrical cross section DFA, DFA-650c, and an S-Band elliptical cross section DFA, DFA-340e.

DFA-650c

The purpose of the DFA-650c was to demonstrate the basic principle of elongating the conductive elements of the coupler to achieve serviceable pass-bands approaching the cutoff frequency of a given waveguide standard. The device was designed for WR-650, to match the experimental extraction standard which could be used by the RPM-12a, and have a modest target pass-band between 0.96 and 1.00 GHz. The

design, illustrated in Fig. 3.21, was optimized around a simplified fabrication process which matched a concentric inner conductor at half the height of WR-650 (A) using readily available material sizes which include: 1.27 cm (0.5 in) thick plate (B), 2.54 cm (1 in) radius bar stock (C), and 0.95 cm (0.375 in) radius bar stock (D). The top conductor with radius (D) had to be inset 0.32 cm (0.125 in) (E) in order to allow (A) to equal 8.3 cm (3.25 in). The remaining variables, which included the length of the top conductor (F), the axial offset of the bottom conductor (G), and the length of the bottom conductor (H), were numerically varied in a HFSS optimization script to achieve a maximal pass-band.

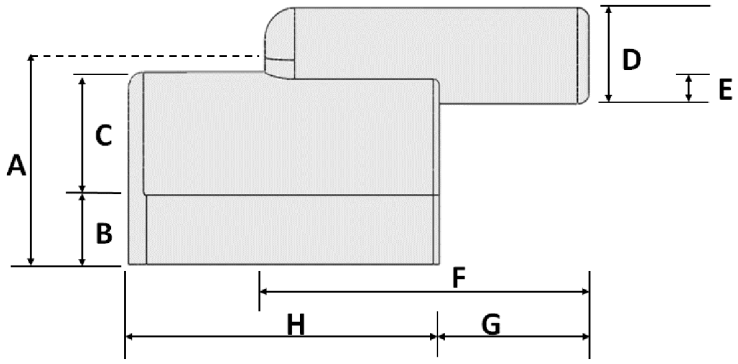

Figure 3.21. Longitudinal cross section (YZ) of the DFA-650c featuring the prominent dimensions used for design and fabrications.

The result of the optimization set F at 6.1 cm, G at 2.8 cm, and H at 6.6 cm and produced a pass-band between 0.93 GHz and 1.08 GHz wherein the VSWR is less than 2. Fig. 3.22(A-B) shows the S(2,1) and VSWR for the frequency band of interest.

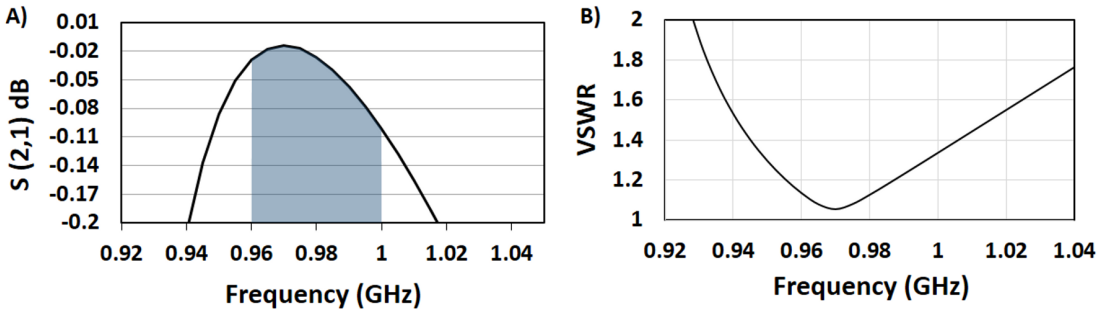

Figure 3.22. Transmission properties of the DFA-650c with: A) S(2,1) as a function of frequency and target frequency band (shaded blue), and B) VSWR as a function of frequency.

VSWRs as low as 1.2, a standard for most commercial products was observed between 0.955 and 0.985 GHz. The full region of interest (0.96 - 1.00 GHz) maintained a simulated VSWR less 1.4, corresponding to a reflection of approximately 2.75 % of incident power.

The simplified geometry of the cylindrical cross section DFA results in minimal reduction in field enhancement as compared to a simple inductive loop. Peak fields of 10 MV/m for input powers of 10 MW and 32 MV/m at 100 MW input power were observed in simulation.

DFA-340e

The DFA-340e, in a manner similar to that of the DFA-650c, uses an adaptation of a two-step, staircase impedance transformer. Additional stages can be used to increase bandwidth at the cost of complexity both in design and fabrication. The bottom conductor, which is bisected by the H-plane of the rectangular waveguide, consists of an initial elliptical cross section with eccentricity ϵ_1 and major radius rm_1. The conductor is centered within this plane and is offset from the back of the waveguide by a distance (a). The structure is linearly tapered to a larger elliptical

cross section of eccentricity ϵ_2 and major radius rm_2, over an axial length (b). This larger cross section axially extends for length (c), after which the structure is terminated by revolving the same cross section about a radius r_1 into the H-plane of the waveguide. Similarly, the top conductor is subject to the same general form and defined by the variables (ϵ_3, rm_3, d, e,ϵ_4, rm_4, f, and r_2), respectfully in Fig. 3.23 (A-B). These variables were analyzed in HFSS to achieve broadband transmission and minimal electric field enhancement.

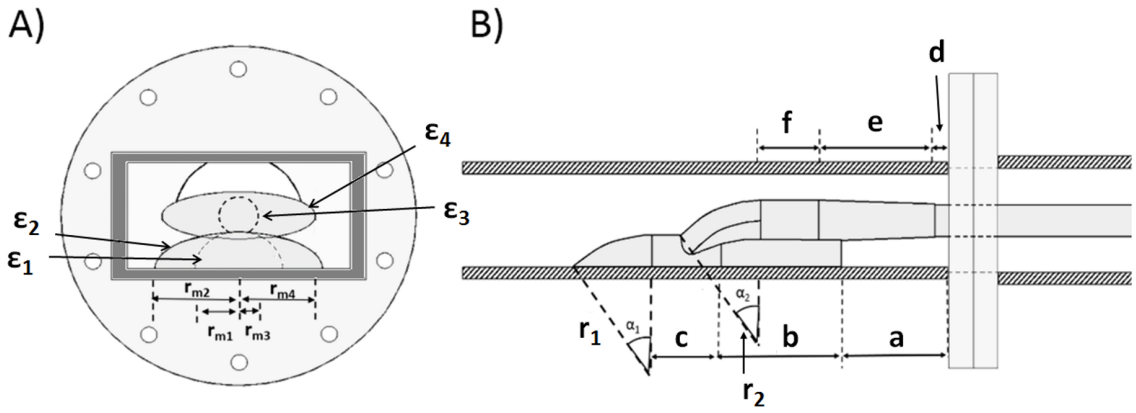

Figure 3.23. A) Transverse cross section of the elliptical DFA with relevant dimensions, and B) Longitudinal cross section of the elliptical DFA with relevant dimensions shown in Table 3.2.

The final design used in the RPM-CACE was the DFA340e prototype whose target design was 1.9 GHz in WR340 waveguide. Figure 3.24 illustrates the transmission properties of the DFA-340e.

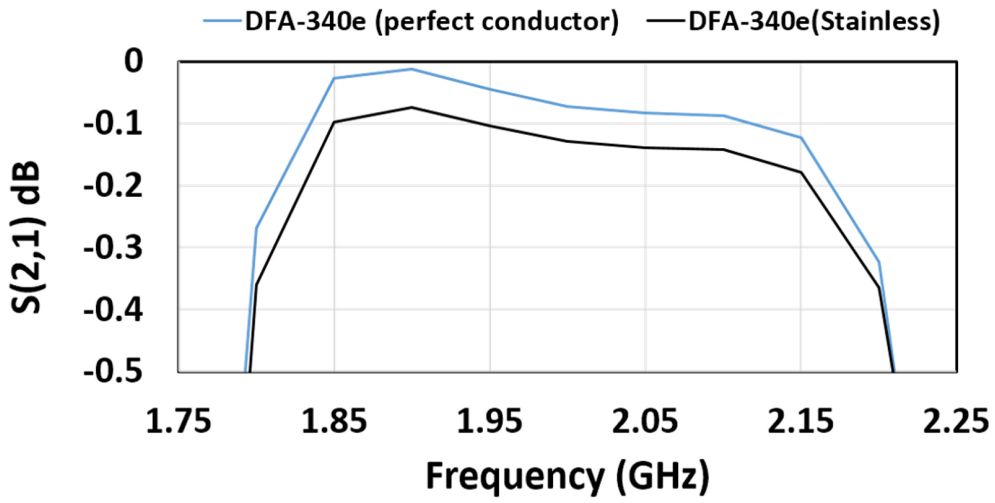

Figure 3.24. Transmission properties of the DFA-340e featuring the two-port S(2,1) parameter as a function of frequency for both a perfect conductor (blue) and a SS coupler (black).

The elliptical DFA has demonstrated transmission bandwidths in excess of 35 % in simulation with VSWR between 1.05 and 1.5. The DFA-340e is a narrow band prototype (20 %) and designed to maximize transmission over the target band between 1.85-1.95 GHz rather than broadband operation. Additional consideration was given to the sensitivity of the couplers dimensions to slight alterations which may be incurred during a physical manufacturing process and assembly. Sensitivity tests, also performed in HFSS, analyzed each optimized variable, from the initial study, by varying its value 5 % and comparing the VSWR at 1.9 GHz as a comparative metric. Variables which demonstrated acute influence (5 % shift in variable value creating more than a 5 % shift in VSWR) to the couplers transmission properties were altered, at the cost of bandwidth and peak transmission, to values of lower sensitivity in order to ensure a realistic physical model could be derived from the study. The plot in Fig. 3.25 compares the peak electric field on the surface of a standard inductive loop coupler with the peak electric field on the surface of the

DFAe as a function of transmitted microwave power from 0 to 200 MW. According to these simulated data, the DFA is capable of transmitting roughly 4 times the power in order to produce the same peak electric field as the standard loop coupler. Figure 3.25 also compares the same DFA-340e models to similar prototypes using the cylindrical and rectangular design architecture shown in Fig. 3.20(A-C).

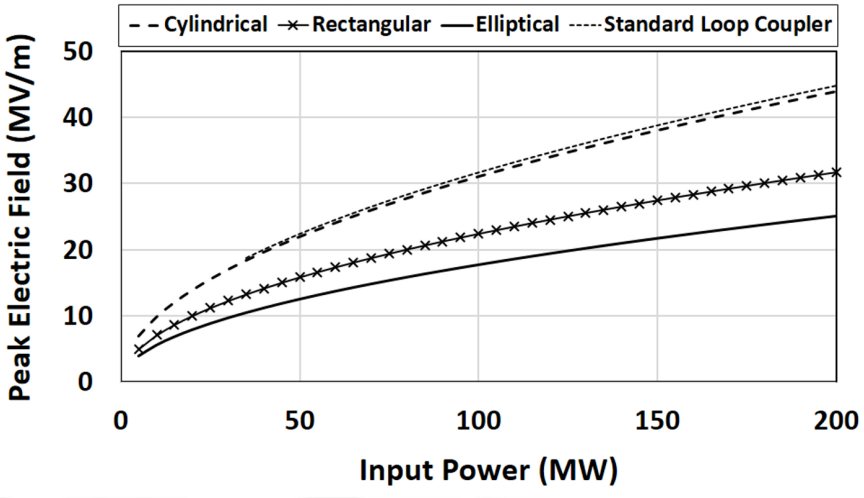

Figure 3.25. Peak Electric field magnitude in the transmission line observed in HFSS as a function of input power.

Simulated data also suggest that the power handling of the coupler increases substantially with increasing size of waveguide housing the device. Using a linearly scaled size and frequency of the DFA-340e, models were generated for both WR-650 and WR-430 in HFSS. Provided a peak input power of 2 GW, field magnitudes of 37 MV/m, 46 MV/m, 73 MV/m were observed for WR-650, 430, and 340 respectfully. The dimensions used for the DFA-340e, which is to be included in the RPM-CACE experiment are shown in Table 3.2.

Table 3.2. Optimized dimensions of the DFA-340e for transmission and minimal electric field magnitude from 1.85 to 2 GHz.

Parameter	Value (cm)	Parameter	Value
a	6.6	ϵ_1	0.33
b	6.2	ϵ_2	0.47
c	3.5	ϵ_3	1.00
d	1.36	ϵ_4	0.325
e	6.0	rm_1	1.7 cm
f	3.0	rm_2	3.2 cm
r_1	5.0	rm_3	0.75 cm
r_2	5.0	rm_4	3.0 cm

3.2.2 Proof of Principle Extractor

The proof of principle extractor model is based on the concept of using an antenna attached to a vane of the magnetron to excite a coaxial transmission line, similar to the extraction method commonly used in the conventional oven magnetron [62] . The system allows for the RF voltage of the central vanes, on each side of the RPM, to drive symmetric coaxial transmission lines as shown in Fig. 3.26(A-B).

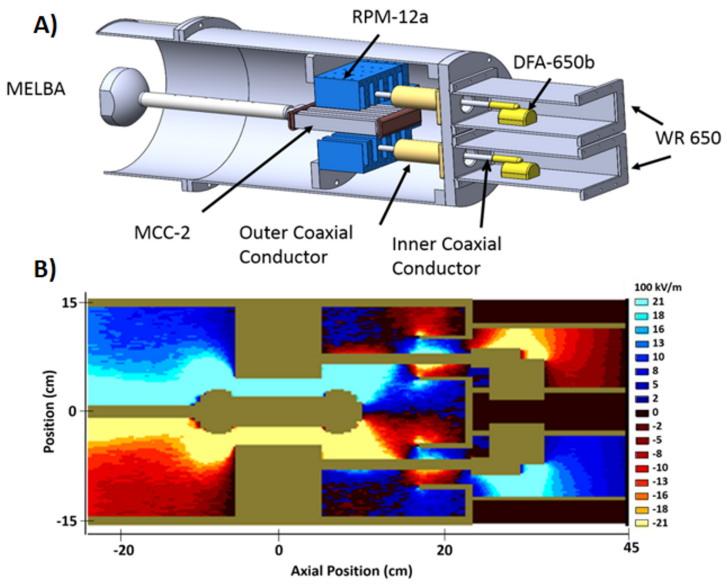

Figure 3.26. A) An oblique 3D rendering of the PoP extractor simulated/experimental configuration made in Solidworks, and B) longitudinal (YZ) cross section of the simulated geometry in MAGIC PIC overlaid with a contour map representing E-field magnitude.

Each coaxial line allows power to propagate out of the chamber and into a standard rectangular waveguide, in this case WR-650, using the DFA-650b in line coupler. Power is then measured from the waveguide RF fields using a Poynting flux plane downstream from the coupler. This model which operated using a -300 kV pulsed and 0.16 T axial magnetic field is summarized in the shot profile illustrated in Fig. 3.27.

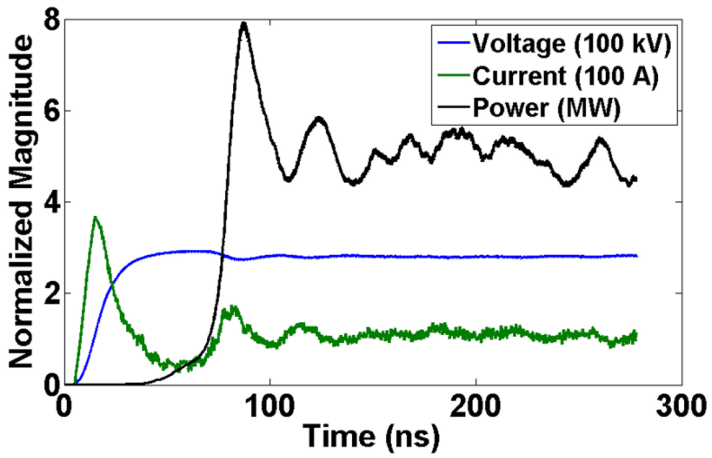

Figure 3.27. Simulated shot profile from MAGIC PIC illustrating voltage (blue), current (green), and extracted power (black) as a function of time.

Figure 3.27 demonstrates extracted power of approximately 5 MW into each waveguide for a total of 10 MW output power. The resultant frequency-pull caused by the addition of a load onto the device is approximately 10 MHz bringing the π-mode frequency from 1.002 GHz to 0.989 GHz as shown in Fig. 3.28. The simulation, which drew only 120 A at 300 kV voltage, demonstrated an efficiency of 28 % which is on par with many relativistic magnetrons [6, 14]. Higher current draws and larger parasitic losses due to effects such as plasma formation, gap closure, and electron

endloss current are not accounted for in simulation.

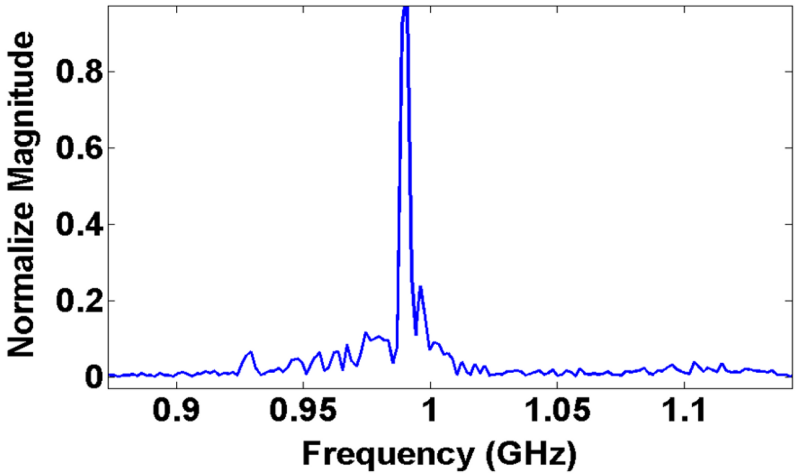

Figure 3.28. Time integrated Fourier Transform of the oscillatory voltage signal within the extraction waveguide.

More efficient coupling schemes could be designed from the PoP extraction scheme by incorporating more vanes into the excitation of the coaxial transmission line or sampling the RF voltage of each vane closer to the AK gap where the RF potential is at a maximum. Proper consideration must be given to these supplementary extraction techniques as they will lower both the Q and resonant frequency of the device. The PoP extractor was designed for WR-650 as it is the largest waveguide that would fit the experimental setup depicted in Fig. 3.26A which has a cutoff frequency at 0.91 GHz. The impedance of modes approaching this cutoff frequency further limit the effective coupling between coaxial transmission lines and waveguide using the DFA. According to Fig. 3.22 the DFA-650c has a pass-band between 0.93-1.08 GHz, which establishes the maximal frequency pulling that can be imposed by the extraction network.

3.2.3 Coaxial All Cavity Extraction (CACE)

The all cavity extractor is based on the concept of reciprocity of the slotted waveguide antenna by which an axially oriented output waveguide is excited by an orthogonal radiation pattern produced by the magnetron [63]. The All Cavity Extractor was originally designed to conform to the azimuthal cavity array of a cylindrical magnetron using double baffled waveguides operating in the TE_{11} mode. Each output waveguide in this configuration is physically spaced by the arc length $\alpha = \frac{4\pi r_a}{N}$, where r_a is the out anode radii and N is the total number of cavities, allowing for ample separation between adjacent extractors. The UM Titan-A6 magnetron, a six cavity, L-band oscillator, utilized this π-primed periodic extraction in simulation using three H-Plane oriented double baffled waveguide (WR-650) [64]. Each waveguide in this assembly, where r_a=8 cm, was spaced 16.8 cm apart allowing for an additional 8.5 cm between extractors for the inclusion of fixtures and flanges.

Planar Arrays

Adapting this concept to the RPM, in a Cartesian configuration, is most intuitively accomplished using the TE_{10} mode of standard rectangular waveguides placed end to end, as demonstrated by the graphic in Fig. 3.29.

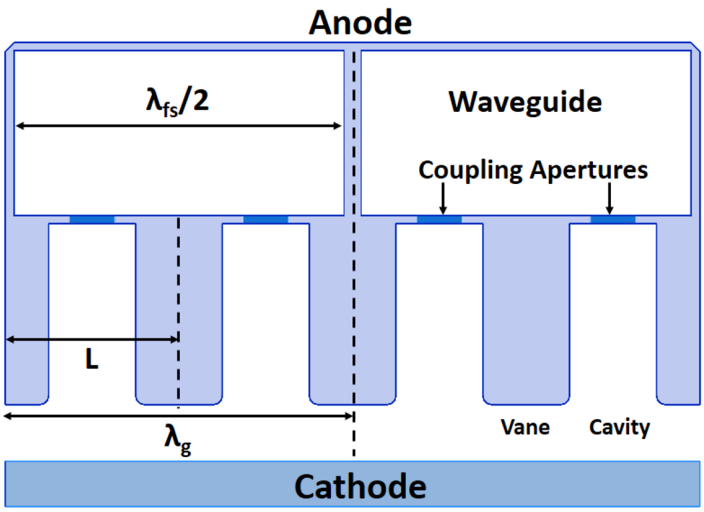

Figure 3.29. A 2D cross-section an all-cavity extraction anode using standard rectangular waveguide.

This conventional approach to the all cavity extractor presents an environment, wherein the transverse dimension of each extractor (d) is now proportional to the periodicity of the planar cavity array (L) by $d = 2L$. This periodicity is related to the guided wavelength ($\lambda_g = (N/n)L$) of mode (n) and total number of cavities (N) or $\lambda_g = d = 2L$ for π-mode operation (assuming negligible waveguide wall thickness). The phase velocity of the magnetron can also be related (d) by $v_{synch} = \lambda_g f_0 = df_0$ where f_0 is the operating frequency. The minimal RF phase velocity, given these approximations, can be shown to be 0.5 c (c is the speed of light) by setting the operation frequency (f_0) equal to the TE_{10} cutoff frequency ($f_0 \approx f_c$) where (d), by nature of rectangular waveguide, may be represented as half a free space wavelength (0.5 λ_{fs}). Realistic estimations of waveguide wall thickness and operating frequencies will significantly increase the estimated phase to approximately 0.65-0.7 c. High phase velocities have deleterious effects on magnetron efficiency, as a highly relativistic beam is now required to achieve synchronism with the wave. In the best

case scenario, only the kinetic energy of the beam required to attain synchronism is lost to the anode and, by conservation of energy; the remaining potential energy, described in Eq. 3.2, is available to transfer to the RF wave [3]. Equation 3.2 uses the term $\gamma = (1 - v_\phi^2/c^2)^{-1/2}$ as the relativistic factor associated with phase velocity (v_ϕ) of the mode and V_0 is the externally applied potential for the diode.

$$\eta_{max} = 1 - \frac{m(\gamma - 1)c^2}{eV_0} \tag{3.2}$$

The peak electrical efficiency of the RPM is plotted versus the synchronous electron beam velocity in Fig. 3.30. Beam velocities in excess of 0.65 c show a peak efficiency of less than 46 % as opposed to a more favorable velocity of 0.3 c which may theoretically achieve 92 % efficiency.

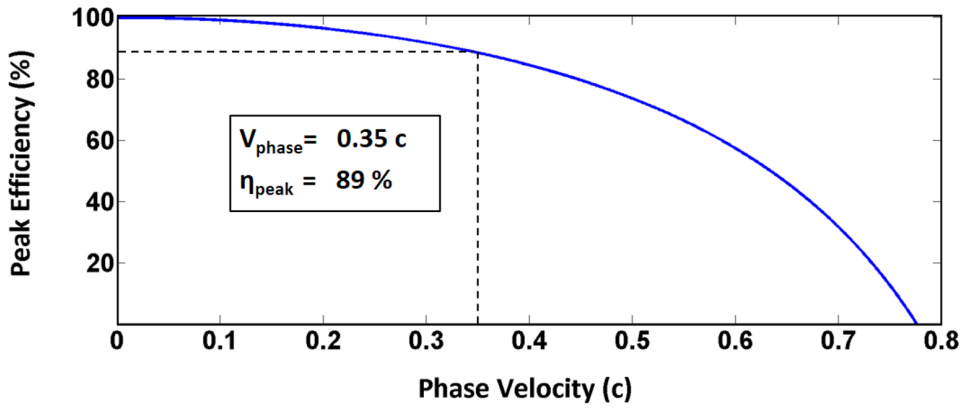

Figure 3.30. Theoretical peak efficiency for magnetron operation as a function of the device's RF phase velocity.

Lowering the RF phase velocity can be accomplished by either decreasing the transverse length (d) of each waveguide or lowering the waveguide's lowest order cutoff frequency. Two proposed solutions to reaching the target velocity of 0.3 to 0.35 c,

using the All Cavity Extractor technique, include implementing capacitively loaded ridged waveguide extractors [65], or converting to the TEM mode in a coaxial transmission line (CTL). The use of a ridged waveguides would effectively lower the cutoff frequency of the extraction waveguide and allow for the use of narrower waveguides when extracting near this reduced cutoff. Particle-in-Cell simulation studies performed on this system have demonstrated the potential to reduce the phase velocity to ∼0.35 c with efficiencies in the range 45 % [65]. The method, however, requires intense capacitive loading and is subject to a high electric field enhancement due to the closely spaced ridges. Alternatively, the reduction of phase velocity may also be achieved by converting to the fundamental TEM in a coaxial transmission line. Since the TEM mode has no cutoff frequency, any radius coax may be used for a given operating frequency and the slow-wave structure may be designed for any desired phase velocity. Coaxial Transmission Lines (CTL), which may be tuned for attenuation, power handling, and impedance are a more versatile option than the ridged waveguides; due to this design flexibility the Coaxial All Cavity Extractor (CACE) was selected over other potential techniques.

3.2.4 CACE Design

The CACE system uses a two stage mode conversion process which couples the TEM mode of two open-face resonant cavities to an orthogonally directed TEM mode in a CTL. The first stage of this process adapts a similar approach as demonstrated in the cylindrical all cavity extractor where the two resonant cavities, operating in pi-mode, excite the TE_{11} mode of a double baffled waveguide with a subtended angle of approximately 120 degrees [64]. The axially oriented TE_{11} mode is geometrically transformed to the TEM mode by gradually folding the waveguide in on itself to form a CTL which is illustrated in Fig. 3.31. This process, as demonstrated in the mode

matched converter, may take several wavelengths in the axial direction to prevent impedance mismatch and reflection [66]. The coaxial all cavity extractor shortens this process by selecting a high reflex angle ($\phi \approx 350^o$) for the initial stage of baffled waveguide. The TE_{11} mode may then be coupled in to what is effectively the final stage of a mode matched converter and excite the TEM mode within $\lambda_{fs}/4$.

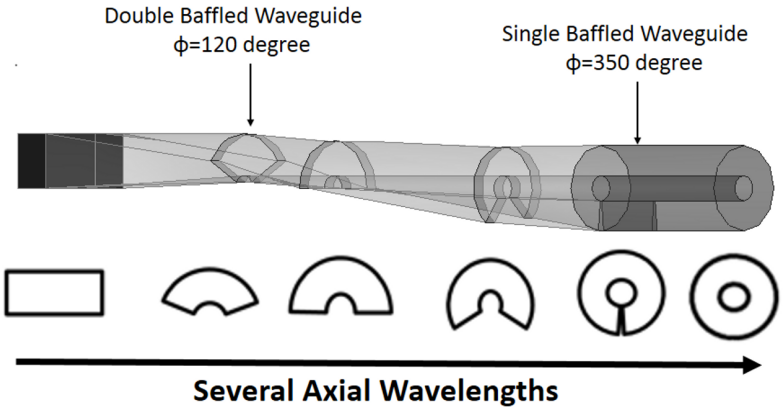

Figure 3.31. Mode Matched Converter: Oblique perspective of 3D model (top) and 2D transverse cross sections at varies stages (bottom).

The initial stage of the CACE output transmission line, shown in Fig. 3.32(A-B), is a single baffled waveguide composed of: an outer conductor (1), inner conductor (2) and baffle (3). Rectangular coupling slots (4) are used at the back-wall of adjacent cavities (5) to couple the RF electric field on either side of the anode vanes (6). Each periodic structure, shown in Fig. 3.32(A-B), is repeated end to end to form a single slow-wave structure of the RPM-CACE. Top and bottom slow wave structures are separated by a distance determined by the AK gap (7) and the cathode (8) thickness. RF power coupled into the output transmission line is mono-directionally propagated in the $\hat{z}$ direction, away from the power supply, using a capacitively-matched shorting

plate (9).

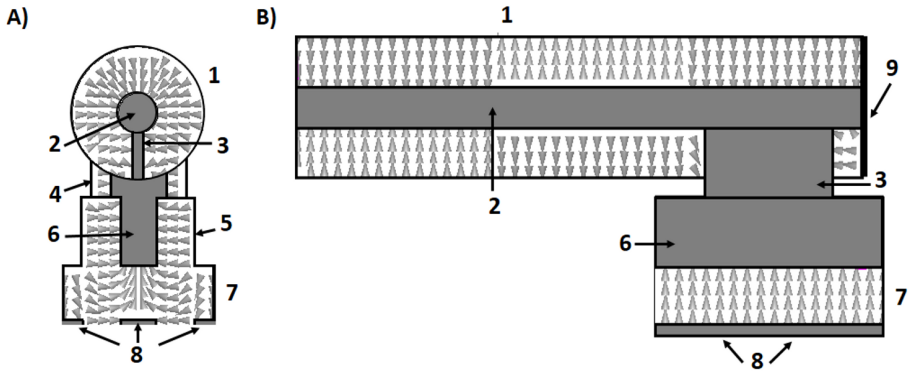

Figure 3.32. Electric field configurations (arrows) for the RPM CACE for the: A) Transverse cross section, and B) Longitudinal cross section.

The baffle itself is electrically connected to both the inner coaxial conductor and is typically designed to be the same axial length as the coupling slot such that the CTL is formed within the axial extent of the anode. The TE_{11} mode that is coupled into the baffled section of waveguide mode converts to the TEM mode of the coaxial transmission line over approximately the same length scale. This mode conversion is theoretically bounded by the cutoff frequencies for the TE_{11} mode in both the baffled waveguide and CTL. The magnetron must operate at a frequency above the TE_{11} cutoff of the baffled waveguide, which is analytically derived from equations 3.1(a-b), to propagate power from the cavities to the CTL. Equation 3.3 (a-b) describes the radial (3.3a) and azimuthal (3.3b) electric field quantities for a baffled waveguide. These relations can be used to determine the cutoff frequency of the TE_{mp} mode for a geometry with an inner radius (ρ_1) and outer radius ($\rho = \rho_2$) for a subtended angle of waveguide equal to (θ) (where $n = m/\theta$ and m is the azimuthal mode number)

[67],

$$E_\rho = \frac{n}{\epsilon_0}\frac{1}{\rho_2}[N_n(k_\rho\rho_2) - \frac{N_n'(k_{\rho_2}\rho_1)}{J_n'(k_\rho\rho_1)}J_n(k_\rho\rho_2)]sin(n\theta)e^{-jk_zZ}, \tag{3.3a}$$

$$E_\theta = \frac{k_\rho}{\epsilon_0}[N_n'(k_\rho\rho_2) - \frac{N_n'(k_\rho\rho_1)}{J_n'(k_\rho\rho_1)}J_n'(k_\rho\rho_2)]cos(n\theta)e^{-jk_zZ}. \tag{3.3b}$$

The TE_{11} cutoff within the coaxial transmission line, characterized by simplified expression in Eq. 3.4, acts as an upper bound to the magnetron operating frequency in order to preferentially excite the TEM mode and inhibit losses and reflection.

$$f_c = \frac{c}{\pi(\rho_1 + \rho_2)\sqrt{\mu_r\epsilon_r}} \tag{3.4}$$

The final stage of the CACE extractor allows for the TEM mode of the CTL to mode convert to the TE_{10} mode of a rectangular waveguide via the in-line DFA, axially downstream from the diode. The system exploits the azimuthal symmetry of coupler to support a rotated (E-plane orientation) waveguide configuration which reduces the transverse extent of the rectangular extractor by a factor of two. The more compact transmission line network supports an RF phase velocity as low as 0.25 c, as opposed to the 0.5 c phase velocity required without the CACE system.

Anode

The RPM-CACE anode block was designed to operate using existing experimental equipment at the University of Michigan which inherently presents some geometric limitations. The 43.2 cm ID of the cylindrical electromagnets allows for the use WR-340 (or smaller) for the output waveguide configuration. The RPM-CACE was established about this largest size waveguide for the purposes of dealing with plasma expansion, electrical breakdown, and ease of access within the transmission line itself.

Given the E-plane width (4.32 cm) of each waveguide, a slow wave structure period

(L) was set at 2.8 cm such that 1.3 cm could exist between each output waveguide. A period of 2.8 cm sets the guided π-mode wavelength at 5.6 cm and bounds our available phase velocity to 0.32 c at the TE_{10} cutoff or 0.65 c at the TE_{20} cutoff. A realistic target of 1.9 GHz was chosen to both minimize the RF phase velocity (0.35 c) and maintain a reasonable separation from the waveguide cutoff (9 %) in order to safely propagate power out of the system. The target operating frequency was established by identifying a structure with an unloaded cold resonance above our targeted value at 2.25 GHz. The unloaded resonant structure housed 12 rectangular resonant cavities, 2.55 cm X 1.4 cm, and extended 8.4 cm in the axial direction. Using a combination of HFSS and ICEPIC [68] the external loading is increased, to induce a frequency pulling effect, by extending the length of a fixed width (1.1cm) rectangular coupling slot. Increasing the coupling of the extractor will inevitably load the anode and lower the quality factor (Q) of the device and reduce the frequency [69], shown in Fig. 3.33, and increase the susceptibility for an over-moded cavity. The goal of this process was to pull the resonant frequency reasonably close to our target while maintaining a quality factor above the over-coupled value, determined in ICEPIC to be around 15. A coupling slot length of 4.8 cm which provided a Q of 40, well above our critical coupling criteria of ($Q = 15$). The resonant frequency of this loaded structure was pulled to roughly 1.98 GHz, which during operation has a beam loaded resonance at 1.9 GHz.

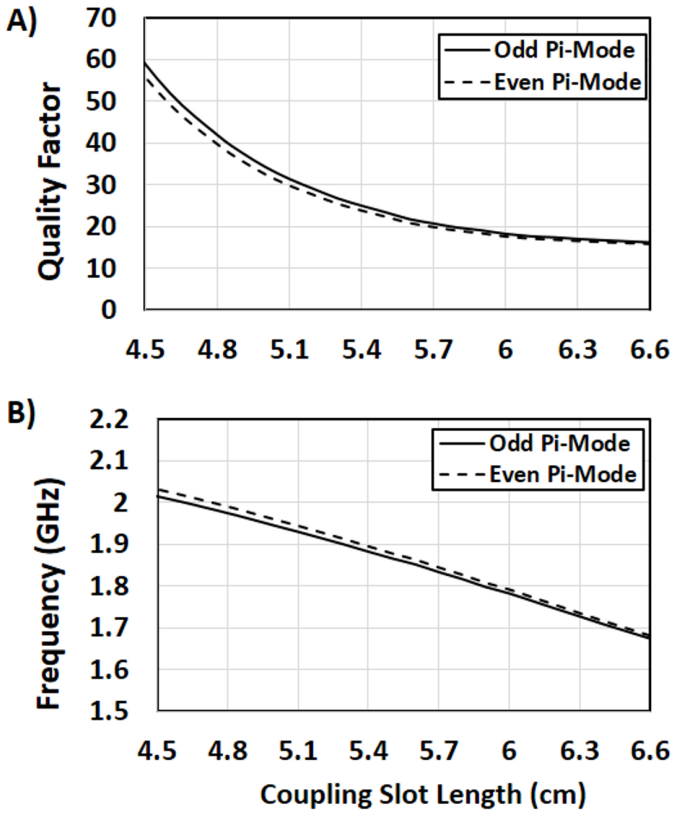

Figure 3.33. Plots correlating: A) the quality factor, and B) the pulled resonant frequency as a function of the length of the RPM coupling slot.

The simulated cold tests shown in Fig. 3-33 were performed in HFSS using a bi-directional coaxial transmission line that extended in both $+\hat{z}$ and $-\hat{z}$. Realistically, in a physical environment, it is advantageous to couple the extracted microwaves away from the power supply and toward a given target in the $+\hat{z}$ direction relative to the supply. This mono-directional coupling is accomplished by installing a simple shorting plate at a given distance (Z_1) from the center of the coupling slot as depicted in Fig. 3.34A. The shorting plate acts to reflect power traveling in the $-\hat{z}$ direction and, if properly designed, constructively interfere with the forward $+\hat{z}$ directed power

and cummulatively add to the net output power in this direction. The installation of the shorting plate also impacts the coupling of the extractor itself, resulting in changes to both the resonant frequency, Fig. 3.34B and the Q of the anode, Fig. 3.34C. Using the quality factor of the RPM as a metric, a distance Z_1 is selected which imposes the same loading on the RPM anode as the bi-directional geometry. The RPM-340CACE demonstrated a bi-directional Q of appoximately 38 which is matched at both $Z_1 = 3.5$ cm and $Z_1 = 7$ cm corresponding to a 1/4 and 1/2 free space wavelength (λ_{fs}) standing wave between the slot and the shorting plate respectfully. Since the reflection coefficient of a conductive short is Γ=-1, the approximate quarter wavelength stub results in the highest power out of the device.

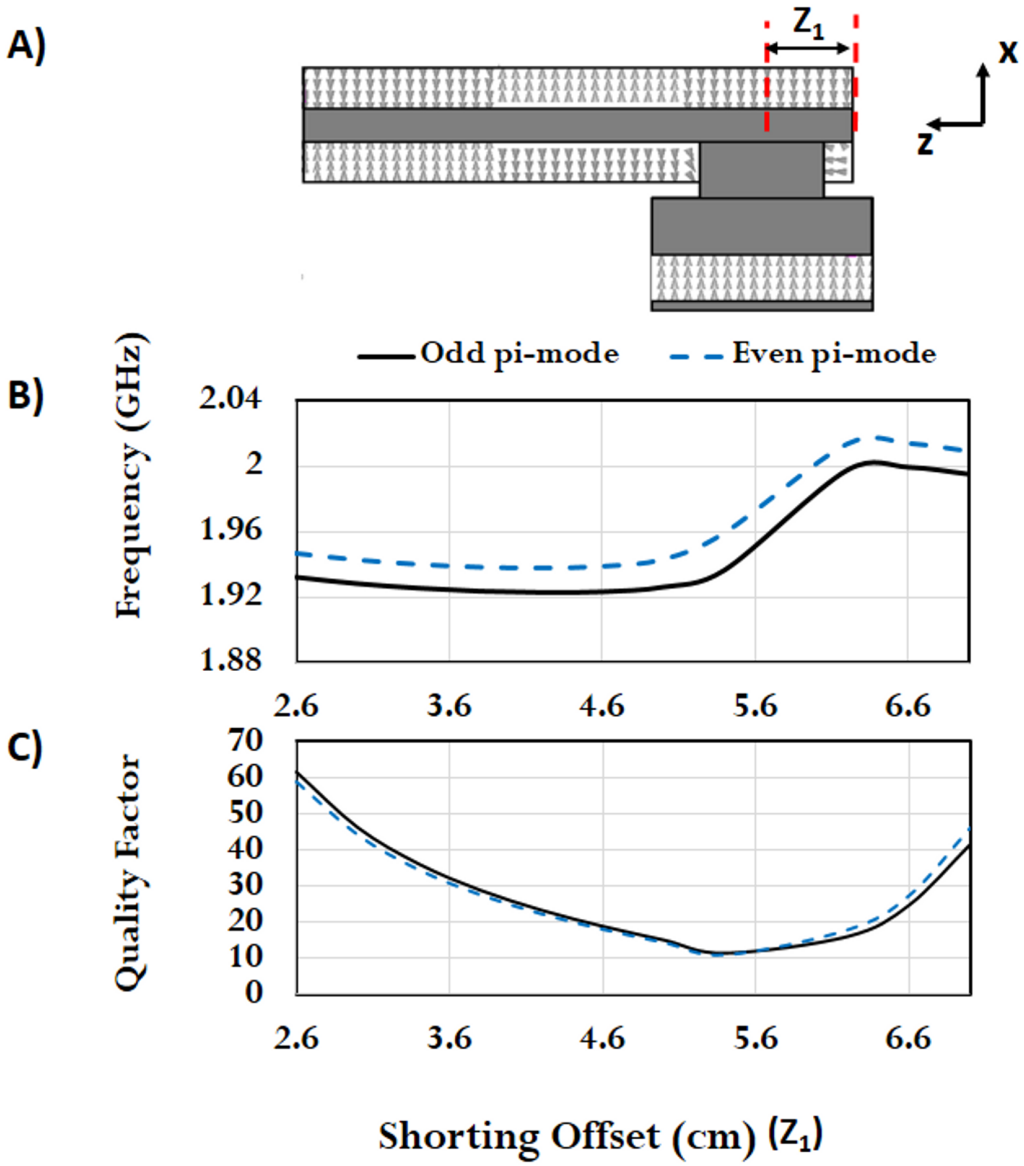

Figure 3.34. A) RPM-340CACE longitudinal cross section (XZ) illustrating the shorting plate offset (Z_1), B) The shift in resonant frequency of even and odd π-modes as a function of Z_1, and C) The shift in quality factor (Q) as a function of Z_1 for both the even and odd π-modes.

Cathode

The full, cold tube, dispersion relation, shown in Fig. 3.35, follows the same parabolic form as any periodic cavity array with the additional split mode structure due to the 2 fold symmetry of the RPM. Modifications due to external loading and the capacitive matching of the shorting plate result in a translation of the frequency of each mode of the dispersion curves but does not heavily impact mode separation between even and odd π-mode.

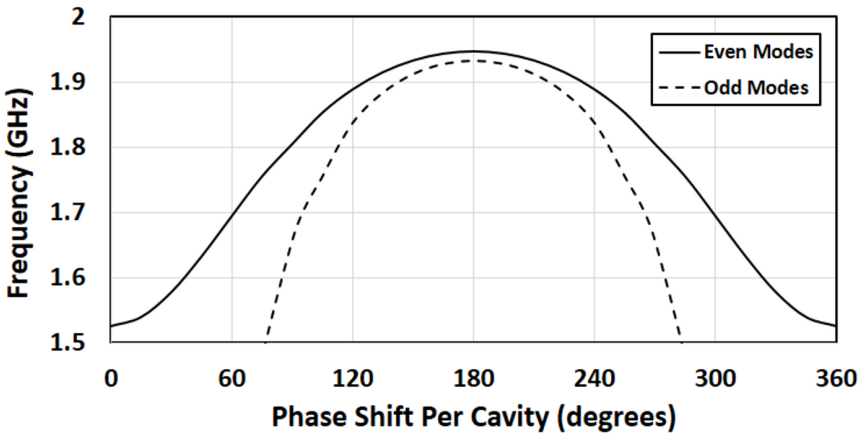

Figure 3.35. Dispersion relation for the RPM-CACE illustrating frequency for the even (dashed line) and odd (solid line) modes as a function of phase shift per cavity, obtained from HFSS.

This baseline simulation was performed employing a standard MCC geometry where by each of the conducting strips of the cathode had the same width (1.4 cm) and period (2.8 cm) of the slow-wave structure. Each planar slow-wave structure of the RPM CACE is separated by 4.5 cm to allow for a 2 cm AK gap and a 0.5 cm thick cathode. The cathode was designed to be 20 cm in total length and is bounded by cylindrical endloss inhibitors which have a 2 cm OD to mitigate axial parasitic current losses. The 2 cm AK gap was chosen as a means to balance fast mode development with potential gap closure due to plasma expansion during operation. Recent the-

ory also suggests that minimizing the thickness ($2h_2$) of the Mode Control Cathode geometry increases mode separation between the even and odd modes [32]. The 15 MHz separation between the even π-mode at 1.97 GHz and the odd π-mode at 1.955 GHz could easily be increased to upwards of 95 MHz by increasing the thickness of the cathode from 0.5 cm to 2.5 cm, which reduces the effective AK gap of the diode to 1 cm. The existing 2 cm gap was chosen to balance mode separation and power feedback through the MCC with the potential for plasma gap closure during the $\sim$ 0.75 μs pulse [70].

Coaxial Transmission Line

The goal of the CTL design was to maintain a peak surface electric field below 20 MV/m or approximately 50 % of the Kilpatrick limit (38 MV/m) for RF powers upward of 100 MW at 1.9 GHz throughout the entirety of the transmission line [71, 72]. Two-surface multipactor within the CTL holds a significantly lower thresholds; however, this phenomenon requires seed electrons to initiate, which can be suppressed for short HPM pulses by using clean, well-polished surfaces, under high vacuum [4, 73]. Mechanically, the minimal wall thickness for a vacuum environment was determined to be 6 mm, which establishes maximal OD at 5 cm. The inner diameter of the coax was tuned to 1.5 cm in order to achieve maximum power handling in the DFA, as shown in Fig. 3.36, while maintaining the necessary frequency limits for operation.

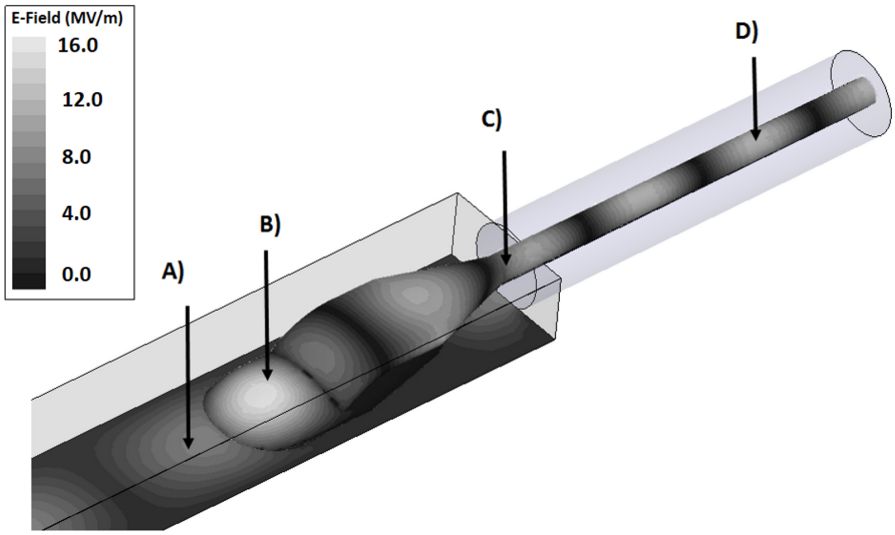

Figure 3.36. Simulated DFAe in HFSS overlaid with contour maps illustrating the peak electric field for 100 MW input power.

Larger inner radii could be used to reduce the field within the coaxial line itself, as demonstrated in Table 3.3, but resulted in a much larger increase in peak fields at the coupler input. Table 3.3 shows the peak electric fields at four distinct points in the DFA-340e transmission line for two assemblies (30 Ohm coax) and (74 Ohm coax). An inner diameter of 1.5 cm, corresponding to a coaxial line impedance of 74 Ohms, provided the optimal balance of peak fields at every point along the coupler.

Table 3.3. Peak Electric Field Magnitudes on the DFA-340e coupler at various point axially along the transmission line.

Position	**30 Ohm (MV/m) (ID = 3cm)**	**74 Ohm (MV/m) (ID = 1.5 cm)**
A	8	8
B	16	16
C	21	15
D	11	14

The primary frequency limit of the output transmission line is defined by the TE_{11} cutoff frequency (Eq. 3.3(a-b)) of a baffled waveguide, above which one must be operate to propagate power from the cavities to the CTL; the TE_{11} cutoff within the coax, should not be exceeded to minimize competition and reflection. The 74 Ohm design satisfies these constraints for a 1.9 GHz operating frequency by setting the TE_{11} cutoff frequency for the baffled waveguide at 1.68 GHz and the TE_{11} cutoff frequency for the CTL at 2.94 GHz.

3.2.5 Particle in Cell Simulations of the RPM-340 CACE

Full 3D hot tests of the RPM-340 CACE were simulated using the particle-in-cell code ICEPIC, Fig. 3.37A [68]. The device demonstrated 450 MW output power at 50 %+ efficiency when operated with a -300 kV pulsed voltage and 0.16 T axial magnetic field, Fig. 3.37B.

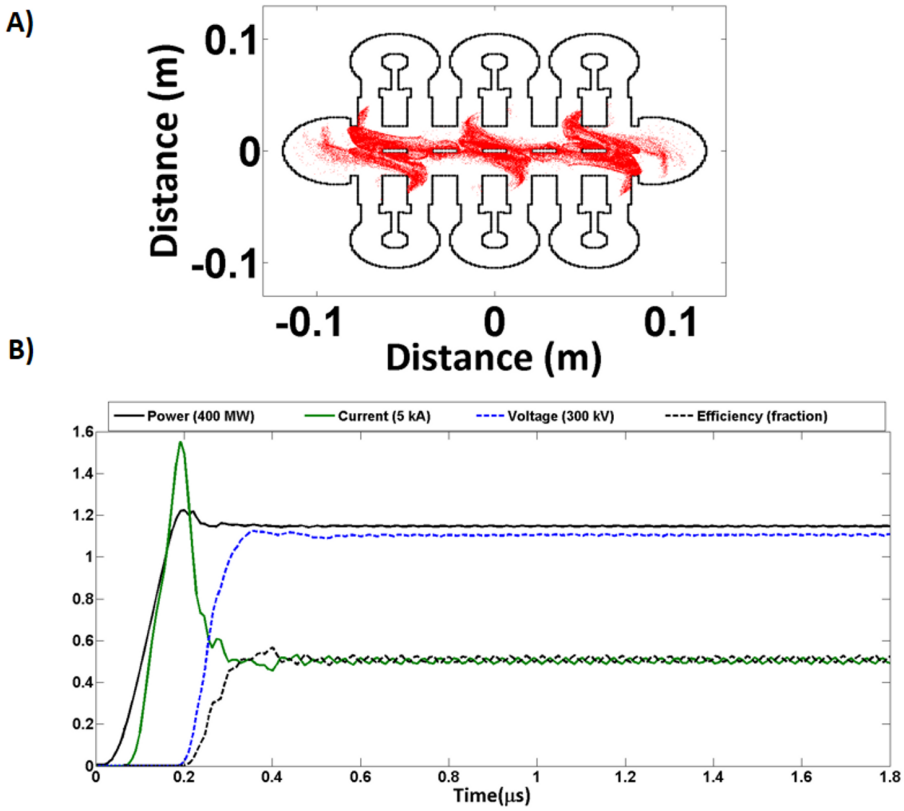

Figure 3.37. A) Phase-space particle plot in ICEPIC representing pi-mode operation of the RPM-CACE with electrons (red) and conducting walls (black) and B) Voltage (dashed-blue), Current (green), Power (black), and Efficiency (dashed-black) as a function of time for the same simulated model.

Higher extracted powers can be attained by expanding the length of the coupling slot [74]. Figure 3.37 (A-B), depicts the simulated peak output power and efficiency for a range of applied magnetic fields.

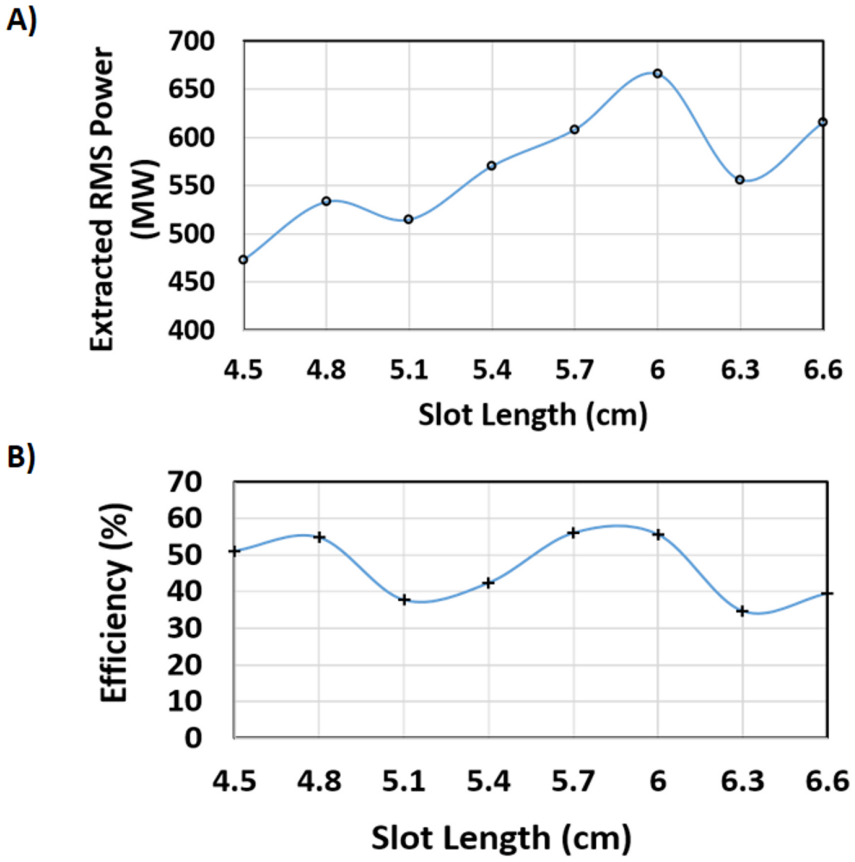

Figure 3.38. A) Total extracted RMS Power, and B) efficiency from the RPM-340CACE as a function of slot length for a fixed width (1.1 cm) rectangular coupling slot.

The total extracted power generally increases as the length of each coupling slot is increased, from 530 MW with the RPM-340 CACE design point at 4.8 cm to 670 MW at a slow length of 6 cm [Fig. 3.38A]. Increasing the slot length past 6 cm decreases the frequency to approximately the WR-340 cutoff at 1.75 GHz and brings the Q of the system down to 15. Power output readily decreases in this regime as the desired mode of operation (even-π) becomes over-coupled and is incapable of supporting proper development. The efficiency of the device was observed to vary in a sinusoidal manner from approximately 35 % to 60 % as slot length was increased,

Fig. 3.38B. The sinusoidal nature of the efficiency can be related to the capacitively matched plate on the back of the baffled waveguide. The placement of this shorting plate is closely coupled to the extractor slot and can adversely affect operation if the standing waveform between the slot and plate is not matched. Extending the slot length linearly caused a cycling of the impedance between the two features which affected both output power and the current drawn by the magnetron.

A slot length of 4.8 cm was chosen to both provide a suitable margin between the operating Q (Q=40) and the over-coupled threshold (Q=15). The peak simulated output power for this coupling slot configuration (4.8cm X 1.1 cm), for high efficiency operation, was observed to be (540 MW) or 90 MW per waveguide. Theoretically, total output power of the device may also be increased by extending the transverse length of the magnetron and including additional extraction waveguides. This modular scalability has been demonstrated in simulation to linearly increase the output power with respect to the number of waveguides while maintaining operating efficiency, frequency, and transmission line field stress.